Academia
Green Energy

10.20935/AcadEnergy8386

Research Article

Analytical framework for structural failure analysis of solar panels subjected to wind loads

Sondipon Adhikari[1,*], Subhamoy Bhattacharya[2]

[1] James Watt School of Engineering, University of Glasgow, Glasgow, UK
[2] Renew Risk, London, UK
* Correspondence: sondipon.adhikari@glasgow.ac.uk

Received: 2 March 2026 | **Accepted:** 17 June 2026 | **Published:** 9 July 2026

Abstract

Introduction: The structural integrity of solar photovoltaic (PV) systems is increasingly threatened by wind-induced failures, with recent extreme weather events exposing the limitations of existing design practices. Although computational fluid dynamics (CFD) and finite element methods (FEMs) are widely employed to simulate wind–structure interaction, their reliance on heavy computation and their limited physical transparency restrict their use as general-purpose design tools.

Materials and methods: This study develops a closed-form analytical framework for the failure analysis of cantilever-mounted solar panels subjected to wind loading. Beginning with a reduced-order mechanical model that captures mast flexibility, panel geometry, and inclination, the framework is developed in three progressively more sophisticated stages: a pseudo-static stress analysis, a static divergence analysis, and a simplified dynamic flutter analysis. Attached flow flat-plate aerodynamics and small-deformation linear elastic structural mechanics underpin all three stages, and a lognormal capacity model is used to derive closed-form fragility functions.

Results: The framework quantifies stresses, deflections, and support reactions under pseudo-static wind loads; identifies the critical divergence wind speed at which destabilising aerodynamic moments overcome structural stiffness; and yields a closed-form ratio $V_{flutter}/V_{div} = 1/\sqrt{2} \approx 0.707$ between the dynamic flutter and static divergence speeds. The closed-form fragility curves provide probabilistic estimates of failure across a range of wind speeds and design configurations, and the parametric expressions demonstrate that mast slenderness, panel inclination angle, and span asymmetry strongly influence critical thresholds for instability and material yielding.

Conclusions: The proposed analytical approach advances understanding by offering a transparent and computationally efficient alternative to simulation-heavy methodologies. The findings support the development of scalable and interpretable design strategies for wind-resilient solar energy infrastructure, thereby complementing numerical and experimental studies and aligning with the broader objectives of structural safety and reliability.

Keywords: solar panel; wind load; structural mechanics; photovoltaic (PV) systems; aeroelastic flutter; fragility curves

1. Introduction

The global shift toward renewable energy has led to an exponential increase in the deployment of solar photovoltaic (PV) systems, both onshore and offshore, as part of the urgent drive to decarbonise energy production. However, as solar farms scale up in size and geographic exposure, their structural vulnerability to extreme wind events has emerged as a significant concern, particularly in the context of intensifying climate variability. In recent years, wind-induced failures of solar panels have resulted in catastrophic economic losses, as seen in some examples **Figure 1**.

(a) (b)

Figure 1. Example of damage to solar panels due to high winds. (**a**) Overturning failure; (**b**) complete damage.

Tornado-induced damage to utility-scale photovoltaic installations was systematically documented in the post-event assessment of Okonkwo et al. [1], who reported module loss, frame failure, and rack overturning across several sites following EF-1 and EF-2 events in the United States. The underlying vulnerability of solar energy infrastructure to extreme wind events has been discussed in the climate resilience literature, notably by Patt et al. [2], who argued that the static wind load prescriptions that govern much of current design practice underestimate the dynamic loading associated with hurricanes and tropical storms. These failures not only threaten grid reliability and energy investment returns but also undermine public confidence in renewable technologies. Despite increasing recognition of these risks, existing engineering standards predominantly rely on static wind load prescriptions and often fail to capture dynamic aeroelastic phenomena such as flutter [3], divergence, and resonance, which are especially critical for slender and elevated solar panel configurations. As the frequency and severity of extreme wind events rise globally, there is a compelling need for a robust and predictive framework to assess the aeroelastic stability and failure probability of solar PV systems under wind excitation. This study addresses this gap through a systematic investigation rooted in structural and aeroelastic dynamics.

A significant body of literature has investigated the influence of wind loads on photovoltaic (PV) panel systems using a variety of approaches. Foundational mechanical design principles, including stress analysis under wind-induced loading and modern treatments of multiaxial stress states [4], remain central to many engineering studies. More recent investigations have extended these principles to address the aeroelastic and structural reliability of solar installations. For example, Dai et al. [5] explored strategies for predicting failure thresholds under fluctuating aerodynamic loads, and similar dynamic response questions have been raised for lightweight structural systems.

The fundamental concerns of wind-induced structural deformation have been addressed in experimental [6–9], numerical [10], and simulation-based studies [11–13]. Investigations into ground-mounted and rooftop PV systems have revealed the critical roles of panel spacing, tilt angle, parapet geometry, and support flexibility in determining structural performance during extreme wind events [14]. Suárez et al. [15] analysed how vortex shedding patterns evolve with tilt angle and contribute to fluctuating aerodynamic loads, complementing earlier work on the role of panel deformation in tracking-system performance.

Recent advances have emphasised the use of computational fluid dynamics (CFD) and high-fidelity numerical modelling to simulate the complex aeroelastic interactions in solar structures. Jubayer and Hangan have conducted multiple studies using detailed CFD analyses to explore wind-induced pressures on both individual panels and large arrays under various orientations and terrain conditions [16, 17]. Aly et al. [11] have investigated the role of machine learning in augmenting CFD simulations for more resilient solar farm design, while others have used large-eddy simulations (LESs) to analyse turbulent flow interactions [14]. Reviews by Nan et al. [13] and Chen et al. [12] provide a thorough account of wind-induced vibrations in PV supports, with implications ranging from local panel uplift to global frame failure. The cumulative knowledge from earlier studies, including that of Laha et al. [10], underscores the diversity of deformation mechanisms that must be accounted for in PV system reliability assessments. Despite this growing body of work, the majority of existing studies depend on expensive CFD simulations, direct numerical methods such as finite element analysis, or wind tunnel testing of scaled-up models, which often restrict scalability, reproducibility, and generalised design application.

Recent research has increasingly focused on aeroelastic phenomena in photovoltaic systems, demonstrating the critical importance of wind–structure interaction analysis for solar infrastructure design. Qin et al. [18] conducted comprehensive wind tunnel experiments comparing rigid body and aeroelastic models for large-span flexible photovoltaic support structures, revealing significant differences in wind-induced vibration responses when aeroelastic effects are properly considered. Ren et al. [19] developed deep learning approaches for spatiotemporal wind pressure field prediction on flexible photovoltaic structures, while Frontini et al. [20] identified key parameters influencing aeroelastic responses of single-axis solar trackers. Advanced stability analysis methods have been developed by Cárdenas-Rondón et al. [21, 22], who investigated aerodynamic derivatives for two-dimensional flat solar trackers at various angles of attack and ground heights, while Taylor et al. [23] provided a comprehensive analysis of aeroelastic instability mechanisms in single-axis solar tracking systems. Studies on alternative support configurations have examined cable-truss systems [24, 25], tracking systems [26], and the influence of tilt angles on wind-induced vibrations [27]. Cai et al. [28] investigated the evolution of vibration forms in large-span flexible arrays, while Aly [29] addressed fundamental scaling issues in wind load evaluation. These studies collectively highlight the complexity of aeroelastic behaviour in solar panel systems and the need for sophisticated analytical approaches that can capture the coupled aerodynamic–structural interactions governing system stability. The present study complements this recent body of high-fidelity numerical and experimental work by providing closed-form analytical expressions for the same coupled aerodynamic–structural problem, directly accessible to the practising designer.

While CFD and finite element methods have produced indispensable insights into the aerodynamic behaviour and structural response of photovoltaic systems, high-fidelity numerical methods often function as computational black boxes, offering limited scope for extracting interpretable physical mechanisms or generalisable design principles. The reliance on high-fidelity simulation and scaled experiments, though valuable, poses challenges in uncovering the fundamental dynamics driving aeroelastic instabilities such as resonance, divergence, and flutter. This methodological gap is especially pronounced when it comes to developing reduced-order predictive models that can provide clarity, scalability, and parametric sensitivity. Recent reviews [12, 13] have emphasised the need for physically interpretable frameworks that bridge the divide between computational complexity and engineering intuition. In this context, there is a conspicuous absence of analytical studies that can deliver closed-form insights into the interaction between aerodynamic forces and flexible solar panel structures. The present study addresses this void by offering a principled, mechanics-based approach to aeroelastic modelling of solar panels under wind loading, enabling the derivation of fragility characteristics through transparent mathematical formulations. This paradigm is expected to complement existing numerical and experimental efforts by providing a theoretical scaffold upon which design standards, failure thresholds, and mitigation strategies can be systematically constructed. As a direct consequence of the approach taken here, it paves the way for several key contributions: an analytical treatment that couples mast flexibility with panel aeroelasticity through a closed-form equivalent torsional stiffness, complementing the existing CFD and wind tunnel literature on aeroelastic photovoltaic structures; the derivation of closed-form analytical expressions revealing that dynamic flutter occurs at approximately 70% of divergence speed, establishing flutter as the governing design criterion; the development of closed-form fragility curves enabling probabilistic risk assessment for wind-induced instabilities; and the identification of explicit parametric dependencies showing the panel inclination angle as the dominant stability parameter. These analytical expressions provide transparency into failure mechanisms previously accessible only through numerical methods, facilitating direct incorporation into design standards and broadening access to aeroelastic analysis for the solar engineering community.

The analytical framework introduced here is intended to complement, rather than replace, the design provisions of established wind codes. The pressure coefficients $C_p(\theta)$ used in Section 3.1 (see **Table 1**) are consistent, within typical experimental scatter, with the net pressure coefficients prescribed for flat plates and "signs and other vertical structures" in ASCE 7-22 §29.3 [30] and in Eurocode EN 1991-1-4 §7.4 [31]. PV module qualification under repeated and extreme mechanical loading is itself codified in IEC 61215-1:2021 [32], against which the analytical framework presented here can be used to bound the design wind speeds at which the module-level qualification tests cease to be sufficient. The basic wind speeds employed in the numerical examples (approximately 35–80 m/s) span the range encountered in ASCE 7 risk category II structures in tornado-affected regions of the United States and the equivalent storm wind contours of Eurocode EN 1991-1-4. The conditional fragility curves $P_f(V)$ derived in subsequent sections, expressing $P(\text{failure} \mid V)$, can be combined with the hazard curves embedded in these standards (or with site-specific hurricane or tornado intensity distributions) to obtain unconditional probabilities of failure, providing a direct bridge between the analytical framework developed here and code-based wind design.

This study develops a structured analytical framework to investigate the aeroelastic stability and wind-induced failure mechanisms of solar photovoltaic panels, progressing from simplified to increasingly sophisticated dynamic models. The analysis begins in Section 2, where a reduced-order mechanical model is formulated to capture the essential physical attributes of the solar panel mast system, including geometric non-uniformity, inclination, and wind-induced aerodynamic forcing. Building upon this foundation, Section 3.1 examines the quasi-static deflection and stress distribution under steady wind loads, enabling baseline identification of critical wind speeds that may induce material failure without dynamic amplification. To capture aeroelastic effects beyond static thresholds, Section 3.2 introduces a static divergence analysis, which accounts for the destabilising influence of aerodynamic lift and moment coupling, revealing divergence-type instabilities and associated critical parameters. Recognising that real-world failures are often dynamic in nature, Section 3.3 extends the investigation to include temporal dynamics and inertial effects, allowing the identification of flutter boundaries and resonant amplification phenomena through a linearised stability analysis. Section 5 reflects on the broader implications of these results, particularly in the context of developing interpretable design tools and complementing existing CFD and FEM-based risk assessment strategies. This hierarchical approach not only elucidates the critical failure modes with increasing physical fidelity but also provides an analytically tractable pathway for understanding and mitigating aeroelastic instabilities in renewable energy infrastructure.

Table 1. Pressure coefficient $C_p(\theta)$ vs. inclination angle θ from the ground for flat plate geometries.

Angle θ (degrees)	**Panel description**	**Pressure coefficient $C_p(\theta)$**
0	Horizontal (facing wind)	0.00–0.20
10	Slightly tilted upward	0.25
20	Mild upward tilt	0.50
30	Moderate upward tilt	0.70
40	Strong upward tilt	0.85
50	Steep upward tilt	1.00
60	Very steep upward tilt	1.10
70	Nearly vertical	1.20
80	Almost vertical	1.25
90	Vertical (facing upward)	1.28

2. Materials and methods

This section formulates the reduced-order mechanical model of the cantilever-mounted solar panel system that underpins the closed-form analytical framework. Following the journal's research article structure, it establishes the geometric, material, and aerodynamic inputs (the "materials") and the cantilever Euler–Bernoulli/attached flow aerodynamic/lognormal-fragility methodology used in the subsequent analytical results sections (the "methods").

2.1. Nomenclature

2.1.1. Geometric parameters

h—mast height (m); t_m—mast thickness (m); b—panel depth out of plane (m); ϵb—mast width (m), with ϵ dimensionless; l_1, l_2—panel span lengths from pivot O to free ends C, B (m); $l = l_1 + l_2$—total panel length (m); t_p—panel thickness (m); θ—geometric inclination angle of the panel from the horizontal (rad); $\alpha = \theta + \theta_m + \phi$—effective inclination angle including mast bending rotation θ_m and dynamic twist ϕ (rad); $\gamma_m = h/t_m$, $\eta_{p_1} = l_1/t_p$, $\eta_{p_2} = l_2/t_p$—non-dimensional slenderness ratios.

2.1.2. Material parameters

$E_m = 210$ GPa, $\sigma_{y,m} = 250$ MPa—Young's modulus and yield stress of the structural steel mast; $E_p = 70$ GPa, $\sigma_{y,p} = 140$ MPa—Young's modulus and yield stress of the Aluminium 6061-T4 panel; ρ_p—panel material density (kg/m^3); $\rho = 1.225$ kg/m^3—air density at standard sea level.

2.1.3. Aerodynamic parameters

V—horizontal mean wind speed (m/s); $C_p(\theta)$—net pressure coefficient for an inclined flat plate; $C_L(\alpha) = 2\pi \sin\alpha \cos\alpha$, $C_D(\alpha) = 1.28 \cos\alpha$—attached flow lift and drag coefficients; $C_M(\alpha) = \frac{1}{4}[C_L(\alpha) - C_D(\alpha) \tan\alpha]$—moment coefficient about O; V_{div}—critical torsional divergence wind speed (m/s); $V_{flutter}$—critical torsional flutter wind speed (m/s).

2.1.4. Structural dynamic and probabilistic parameters

k_θ—equivalent torsional stiffness of the coupled mast–panel system (Nm/rad); $\Gamma = 3\gamma_m[\eta_{p_1} + \eta_{p_2}]^2 + \epsilon[\eta_{p_1}^3 + \eta_{p_2}^3]$—non-dimensional flexibility parameter; J_p—panel mass moment of inertia about O (kg m^2); $\phi(t)$—dynamic torsional rotation of the panel about O (rad); $P_f(V) = P(\text{failure} \mid V)$—conditional fragility, the probability of failure given a wind speed V; β—logarithmic standard deviation of the lognormal capacity distribution.

2.2. Formulation of the system model

The idealised model shown in **Figure 2** represents a simplified two-dimensional representation of a solar panel system consisting of two primary structural components: a vertical support mast and a cantilevered solar panel.

The support mast OA forms the primary vertical structural element of the system, where point O represents the pivot or connection point where the solar panel attaches to the support mast, while point A indicates the base of the mast where it is anchored to the foundation. The mast has a total height denoted by h, measured from the foundation level at point A to the panel connection point at O. A critical design parameter t_m represents the thickness or characteristic dimension of the support mast cross-section, which directly influences the mast's flexural rigidity EI and its ability to resist bending moments induced by wind loads transmitted from the solar panel.

The solar panel BC is modelled as a beam extending from the support mast. Point B represents the lower free end of the panel, and it connects to the support mast at point O, while point C indicates the upper free end or tip of the panel. The panel geometry is characterised by several key dimensions: l_1 denotes the span length from point O to point C, l_2 represents the span length from point O to point B, and b represents the panel depth extending out of the plane of the figure, constituting the third dimension perpendicular to the two-dimensional representation shown.

The inclination angle θ defines the panel's orientation relative to the horizontal plane, measured from the horizontal ground plane upward to the panel surface. In this configuration, $\theta = 0°$ would represent a horizontal panel facing the wind, while $\theta = 90°$ would represent a vertical panel. The parameter t_p represents the panel thickness, which affects the panel's structural properties, including its moment of inertia and section modulus for bending resistance calculations. The wind velocity V is represented by horizontal arrows indicating the direction and magnitude of the approaching wind flow, assumed to be uniform and horizontal, striking the inclined panel surface and creating both normal and tangential pressure components.

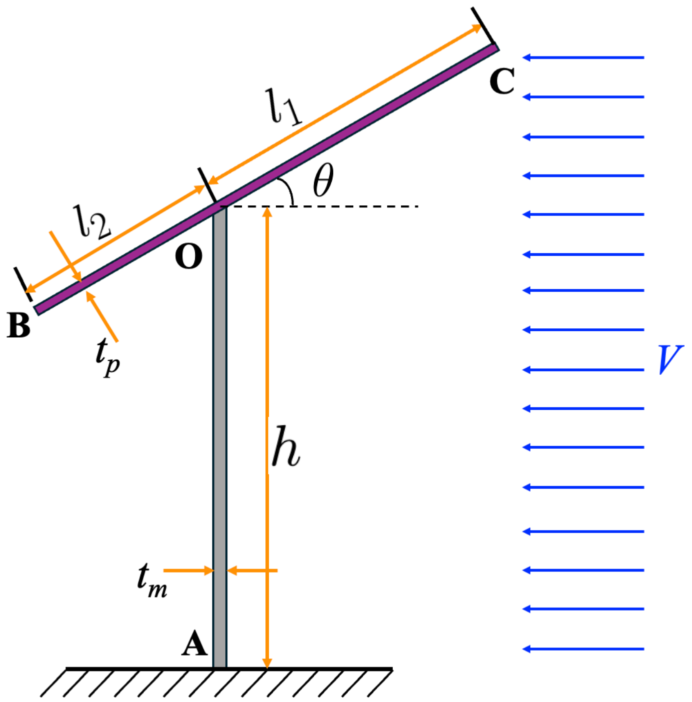

Figure 2. Idealised two-dimensional model of a solar panel structure subjected to horizontal wind loading (denoted by velocity V). The vertical support mast OA has height h and thickness t_m, with point A representing the fixed foundation and point O the panel attachment location. The solar panel extends from B to C with lengths l_1 (CO) and l_2 (OB), panel thickness t_p, and out-of-plane depth b. The panel is inclined at an angle θ from the horizontal, and the system is subjected to uniform horizontal wind velocity V as indicated by the arrows.

This idealised representation incorporates several key simplifying assumptions that enable the application of classical beam theory and aerodynamic analysis techniques. The support mast is treated as a cantilever beam fixed at the base, while the solar panel behaves as a rigid cantilever beam attached to the mast. The model assumes uniform wind loading across the panel surface and analyses the system response in a single vertical plane. Structural connections are assumed to be rigid, and foundation support is considered infinitely rigid. The model establishes a clear coordinate system with the foundation level serving as the reference datum, where the vertical distance h provides the moment arm for calculating overturning moments at the base, while the horizontal projection of the panel creates the primary wind-catching surface area. This simplified model captures the essential structural behaviour and wind–structure interaction phenomena relevant to solar panel systems while maintaining mathematical tractability for analytical solutions.

Throughout the manuscript, two structural materials are assigned. The vertical support mast is modelled as structural steel with Young's modulus $E_m = 210$ GPa and yield stress $\sigma_{y,m} = 250$ MPa, consistent with standard rolled-section steel grades. The solar panel itself, comprising the photovoltaic glass-and-frame assembly, is modelled as Aluminium 6061-T4 with Young's modulus $E_p = 70$ GPa and yield stress $\sigma_{y,p} = 140$ MPa, which is representative of the extruded panel framing used in commercial PV modules. These two assignments are used consistently in all numerical examples: the mast response in Section 3.1.1, the panel response in Section 3.1.2, the divergence analysis in Section 3.2, and the flutter analysis in Section 3.3. The closed-form analytical expressions themselves are material-independent and can be applied to other material combinations (for example, a galvanised steel mast with a glass–aluminium laminate panel, or a fibre-reinforced composite assembly) by substituting the corresponding values of E, σ_y and density.

The closed-form framework rests on the following modelling assumptions, which are recalled at the point of use in each subsequent section: (a) the mast is modelled as a cantilever Euler–Bernoulli beam fixed at the foundation, valid for mast slenderness $\gamma_m \gtrsim 20$ [4]; (b) the panel is modelled as a rigid plate cantilevered from the mast on each side of the pivot O, with bending stresses computed by classical beam theory; (c) all rotations remain in the small-deformation linear elastic regime ($\theta_m, \phi \ll 1$ rad), consistent with the operational range of solar trackers; (d) the aerodynamics is attached flow flat-plate aerodynamics with angle of attack $\alpha \lesssim 20°$, as in [33–35]; (e) the mean wind loading is uniform across the panel surface, consistent with the along-wind correlation length of the atmospheric boundary layer at the spatial scale of a single panel [36]; and (f) the foundation is rigid. The regimes in which these assumptions are not satisfied (large-deformation, stall flutter, turbulent buffeting, foundation–soil interaction, multi-panel array effects) are addressed in the Limitations and Applicability subsection at the end of the manuscript.

3. Results

The closed-form analytical framework formulated in Section 2 is now applied to the cantilever-mounted solar panel system, in three progressively more sophisticated subsections: a pseudo-static stress analysis (Section 3.1), a static divergence analysis (Section 3.2), and a simplified dynamic flutter analysis (Section 3.3). Each subsection both develops the closed-form expressions specific to the relevant failure mode and presents the parametric and probabilistic results that follow from them; this hybrid presentation reflects the inseparable character of derivation and result in an analytical study.

3.1. Pseudo-static analysis

The pseudo-static analysis provides a fundamental assessment of the solar panel system's structural response under steady wind loading conditions. This approach treats the wind-induced forces as static loads applied to the structure, neglecting dynamic effects such as vibrations, resonance, and time-dependent aerodynamic phenomena. While this simplification does not capture the full complexity of wind–structure interaction, it establishes essential baseline results for maximum stresses, deflections, and failure modes under critical loading scenarios.

In this analysis, the structural system is decomposed into its primary load-bearing components: the vertical support mast and the cantilevered solar panel. Each component is analysed independently using classical beam theory to determine critical stress distributions and deformation patterns. The support column analysis focuses on the combined effects of axial loading, bending moments, and potential buckling instabilities arising from wind-induced overturning forces. The panel analysis examines flexural stresses and deflections resulting from distributed pressure loading normal to the inclined surface.

The pseudo-static approach serves multiple purposes in the overall design methodology. It provides conservative estimates for structural sizing and safety factor calculations, establishes reference values for comparison with dynamic analysis results, and identifies critical failure modes that govern the design requirements. Furthermore, the analytical solutions derived from this approach offer computational efficiency and physical insight that complement more sophisticated numerical methods employed in subsequent dynamic and aeroelastic analyses.

 10.20935/AcadEnergy8386

3.1.1. Failure analysis of support column

Figure 3 illustrates the systematic decomposition of wind-induced loading on the solar panel support structure into manageable analytical components. The analysis approach employs classical structural mechanics principles to transform the complex distributed wind loading into equivalent concentrated forces and moments that can be analysed using standard cantilever beam theory.

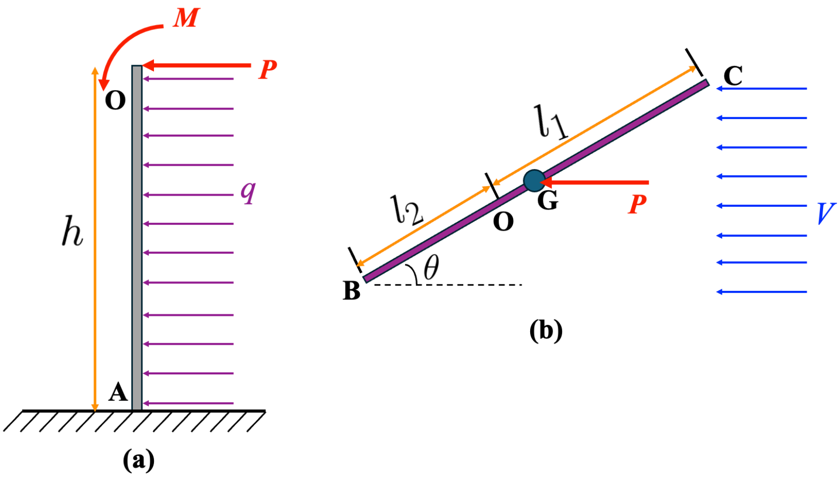

Figure 3. Decomposition of wind loading (denoted by velocity V) on the solar panel support structure for structural analysis. (**a**) The vertical mast OA is modelled as a cantilever beam subjected to concentrated force P and moment M at point O from the panel attachment, plus distributed load q representing direct wind pressure on the mast. The mast has a height h, thickness t_m, and width ϵb, where b is the width of the panel. (**b**) The resultant aerodynamic force P acts at the panel's centre of gravity G, which is, in general, offset from the structural attachment point O, creating the transmitted moment M due to this eccentricity.

The structural analysis employs a decomposition approach based on the distinct mechanical behaviours of the two primary components: the slender mast (governed by beam bending theory) and the panel (governed by plate theory). This separation is physically justified because:

- The mast experiences primarily flexural deformation under lateral loading;
- The panel experiences combined bending and twisting under distributed pressure;
- The connection at point O transmits forces and moments between components.

The rotation compatibility at point O requires that the panel's effective inclination equals the geometric angle plus the mast's rotational deformation: $\alpha = \theta + \theta_m$, where the mast rotation θ_m is determined from standard cantilever beam relationships.

The analysis is structured as a two-stage process that separates the aerodynamic loading from the structural response. The first stage focuses on determining the resultant wind forces acting on the solar panel, as shown in **Figure 3**. The horizontal wind velocity creates a distributed pressure loading across the inclined panel surface. This distributed loading is reduced to a single resultant force P that acts at the panel's centre of gravity, point G. The effective surface area used in the force calculation that follows is the area projected normal to the incoming horizontal wind, $A_{\perp} = b\,(l_1 + l_2)\,\sin(\theta)$, rather than a horizontal or vertical projection of the panel surface. For a vertical panel ($\theta = 90°$), this projected area equals the full panel area $b(l_1+l_2)$, while for a horizontal panel ($\theta = 0°$), it tends to equal zero, in agreement with classical bluff body aerodynamics for cross-flow over a flat plate. The pressure coefficient $C_p(\theta)$ tabulated in **Table 1** is correspondingly defined relative to the dynamic pressure acting on this projected area. This force can be calculated considering that the wind acts on the effective surface area $b \times (l_1 + l_2)\sin(\theta)$ as

$$P = \frac{1}{2}\rho V^2 C_p(\theta)\,(b(l_1 + l_2)\sin(\theta)) \tag{1}$$

where:

- ρ is the air density (kg/m^3).
- V is the horizontal wind speed (m/s).
- $C_p(\theta)$ is a pressure coefficient.

The pressure coefficient is typically obtained empirically or from standard tables for flat plates or panels at an angle θ. Standard values of $C_p(\theta)$ for flat plates are given in **Table 1** (see, for example, [37]). The tabulated values are consistent, to within typical experimental scatter, with the net pressure coefficients prescribed for flat plates and "signs and other vertical structures" in ASCE 7-22 §29.3 [30] and Eurocode EN 1991-1-4 §7.4 [31], which provides a direct mapping between the analytical framework developed here and code-based wind design practice. This preliminary force estimation using pressure coefficients provides conservative values for structural sizing and is appropriate for the support column analysis. A more detailed aerodynamic analysis using lift and drag coefficients is presented later for the panel component, where the complex aerodynamic behaviour requires more sophisticated treatment. The analysis considers only the horizontal force component from the panel because the vertical component induces axial stress in the mast, which is negligible compared to bending stress due to the high axial stiffness of slender columns. Furthermore, vertical forces from wind loading on inclined panels create tensile rather than compressive axial stresses, eliminating concerns about axial buckling that could govern column design. The lateral bending behaviour represents the critical failure mode for wind-loaded mast structures.

In this pseudo-static treatment of the mast, we likewise omit the tangential (in-plane) component of the wind force on the panel. The tangential component on a thin flat plate is dominated by surface skin friction rather than by a pressure differential, and for the Reynolds numbers and surface finishes typical of glass-fronted PV modules ($Re \sim 10^6$, $C_f \sim 0.003$–0.005 for smooth flat plates [33]), it amounts to at most a few percent of the normal pressure force; it would, in any case, act partly in tension and partly in compression at the mast root, with the small residual compressive part being covered by the flexural-compressive buckling check at the end of this section. The full lift and drag decomposition, which retains both components, is reintroduced in the refined panel analysis of Section 3.1.2.

The density of the air is normally taken as $\rho = 1.225$ kg/m^3.

The critical aspect of this stage is recognising that point G does not coincide with point O, the structural pivot point where the panel attaches to the mast. This eccentricity is not introduced for analytical convenience: in practice, single-pole and central-pivot cantilever-tracker installations almost always place the supporting mast off-centre relative to the geometric centre of the panel in order to accommodate a torque tube, hydraulic drive or pivot bearing behind the panel, and to satisfy construction and access tolerances. The symmetric case $l_1 = l_2$ (zero eccentricity, $OG = 0$) is recovered automatically from the same closed-form expression as a special case. This geometric offset creates an additional moment that must be transmitted to the support structure. Assuming $l_1 \geq l_2$ without any loss of generality, the length OG can be determined as

$$OG = \frac{l_1 + l_2}{2} - l_2 = \frac{l_1 - l_2}{2} \tag{2}$$

Therefore, the moment M about the pivot point O is obtained as

$$\begin{aligned} M &= P \times OG \sin\theta = \tfrac{l_1 - l_2}{2} \sin\theta \tfrac{1}{2}\rho V^2 C_p(\theta)\,(b(l_1 + l_2)\sin(\theta)) \\ &= \tfrac{1}{4}\rho b V^2 C_p(\theta) \sin^2(\theta)\left(l_1^2 - l_2^2\right) \end{aligned} \tag{3}$$

For the support column failure analysis, this study employs simplified aerodynamic loading assumptions where the resultant force is treated as acting at the centre of gravity rather than the aerodynamically correct centre of pressure. This simplification is appropriate for preliminary structural analysis of the support column, where the primary objective is determining equivalent static loads for beam design rather than precise aerodynamic modelling. The centre of gravity assumption provides conservative estimates for structural sizing and has minimal impact on column design calculations since the overall panel loading magnitude dominates over the specific force application point.

The second stage examines how the aerodynamic forces from the panel are transmitted to the vertical support mast and subsequently to the foundation, as depicted in **Figure 3b**. At point O, the mast experiences a concentrated lateral force P from the panel and an additional concentrated moment M arising from the eccentricity between points G and O. This moment equals P times the perpendicular distance between these two points. The mast may also be subjected to a distributed load q representing wind pressure acting directly on the mast surface. The mast width is generally smaller than the panel, and it is assumed to be ϵb, where ϵ is a small number. The uniformly distributed load (N/m) q can be obtained as

$$q = \epsilon b \frac{1}{2}\rho V^2 C_p(\theta), \quad \theta = 90^\circ \tag{4}$$

The aerodynamic coefficients used for the panel and mast are obtained from different sources, reflecting their distinct geometries and flow conditions. The panel pressure coefficients $C_p(\theta)$ in **Table 1** are based on experimental data for flat plates at various inclination angles under cross-flow conditions. The mast pressure coefficient $C_p(90^\circ) = 1.28$ represents the drag coefficient for a cylinder or rectangular section in cross-flow, accounting for the different flow patterns around the slender mast geometry compared to the broad panel surface. This distinction is important because the mast experiences primarily cross-flow drag while the panel experiences complex pressure distributions dependent on inclination angle.

The vertical mast is modelled as a cantilever beam with a fixed support at A and a free end at O. The foundation connection at point A is assumed to provide complete restraint against translation and rotation, while the free end at O receives the concentrated force and moment from the panel attachment. The total structural response is obtained by superposing the effects of the concentrated force P, the concentrated moment M, and any distributed load q along the mast length. This superposition is valid due to the linear elastic behaviour assumption and the principle of small deflections. The decomposition approach enables the application of standard cantilever beam solutions for each loading component. As an example, for the concentrated force P at the free end, the maximum deflection occurs at the tip and equals $Ph^3/(3EI)$. The concentrated moment M produces a tip deflection of $Mh^2/(2EI)$. Any distributed loading q contributes an additional deflection of $qh^4/(8EI)$. The total deflection and stress distributions are obtained by algebraically summing these individual contributions. The maximum stress occurs at the root. The bending moment at the root is therefore obtained by superposition as

$$
\begin{aligned}
M_t &= M + Ph + qh^2/2 \\
&= b\frac{1}{2}\rho V^2 \left(2C_p(\theta)\sin^2(\theta)\left(l_1^2 - l_2^2\right) + h(l_1 + l_2)\sin(\theta) + \epsilon h^2 C_p(90^\circ)/2\right)
\end{aligned} \tag{5}
$$

The maximum stress due to this bending moment is given by

$$
\sigma_{\max} = \frac{M_t(t_m/2)}{I_m} = \frac{6M}{\epsilon b t_m^2} \tag{6}
$$

In the above, the flexural rigidity of the mast

$$
I_m = \frac{\epsilon b t_m^3}{12} \tag{7}
$$

and t_m is the thickness of the mast. Substituting the expression of the moment in the equation of maximum stress, we have

$$
\sigma_{\max} = \frac{3\rho V^2}{\epsilon}\left(2C_p(\theta)\sin^2(\theta)\left(\eta_{m_1}^2 - \eta_{m_2}^2\right) + \gamma_m(\eta_{m_1} + \eta_{m_2})\sin(\theta) + \epsilon\gamma_m^2 C_p(90^\circ)/2\right) \tag{8}
$$

Here, the non-dimensional structural parameters for the mast are

$$
\eta_{m_1} = \frac{l_1}{t_m}, \eta_{m_2} = \frac{l_2}{t_m}, \quad \text{and} \quad \gamma_m = \frac{h}{t_m} \tag{9}
$$

Failure is assumed to occur when $\sigma_{\max} \geq \sigma_y$, where σ_y is the yield stress of the material. The total deflection of the pivot point can be calculated by adding the deflections arising from the forces and moment as

$$
\delta_m = \frac{Ph^3}{3EI_m} + \frac{Mh^2}{2EI_m} + \frac{qh^4}{8EI_m} \tag{10}
$$

In the above expression

$$
\frac{Ph^3}{3EI_m} = \frac{1}{6}\cdot\frac{\rho V^2 b h^3}{EI_m}\cdot C_p(\theta)(l_1 + l_2)\sin(\theta) = \frac{2\rho V^2 t_m}{E\epsilon}\cdot C_p(\theta)\cdot(\eta_{m_1} + \eta_{m_2})\cdot\gamma_m^3\cdot\sin(\theta) \tag{11}
$$

$$
\frac{Mh^2}{2EI_m} = \frac{3\rho V^2 t_m}{2E\epsilon}\cdot C_p(\theta)\cdot(\eta_{m_1}^2 - \eta_{m_2}^2)\cdot\gamma_m^2\cdot\sin^2(\theta) \tag{12}
$$

$$
\frac{qh^4}{8EI_m} = \frac{3\rho V^2 t_m}{4E}\cdot C_p(90^\circ)\cdot\gamma_m^4 \tag{13}
$$

Using these, the total deflection is obtained as

$$
\delta_m = \frac{\rho V^2 t_m}{E}\left[\frac{2}{\epsilon}C_p(\theta)(\eta_{m_1} + \eta_{m_2})\gamma_m^3\sin(\theta) + \frac{3}{2\epsilon}C_p(\theta)(\eta_{m_1}^2 - \eta_{m_2}^2)\gamma_m^2\sin^2(\theta) + \frac{3}{4}C_p(90^\circ)\gamma_m^4\right] \tag{14}
$$

In a similar manner, the total rotation of the pivot point can be calculated by adding the rotations arising from the forces and moment as

$$
\phi_m = \frac{Ph^2}{2EI_m} + \frac{Mh}{EI_m} + \frac{qh^3}{6EI_m} \tag{15}
$$

where

$$\frac{Ph^2}{2EI_m} = \frac{3\rho V^2}{E\epsilon} \cdot C_p(\theta) \cdot (\eta_{m_1} + \eta_{m_2}) \cdot \gamma_m^2 \cdot \sin(\theta) \tag{16}$$

$$\frac{Mh}{EI_m} = \frac{3\rho V^2}{E\epsilon} \cdot C_p(\theta) \cdot (\eta_{m_1}^2 - \eta_{m_2}^2) \cdot \gamma_m \cdot \sin^2(\theta) \tag{17}$$

$$\frac{qh^3}{6EI_m} = \frac{\rho V^2}{E} \cdot C_p(90°) \cdot \gamma_m^3 \tag{18}$$

Adding these, the total rotation is simplified to

$$\theta_m = \frac{\rho V^2}{E}\left[\frac{3}{\epsilon}C_p(\theta)(\eta_{m_1} + \eta_{m_2})\gamma_m^2 \sin(\theta) + \frac{3}{\epsilon}C_p(\theta)(\eta_{m_1}^2 - \eta_{m_2}^2)\gamma_m \sin^2(\theta) + C_p(90°)\gamma_m^3\right] \tag{19}$$

This systematic separation of aerodynamic and structural analysis stages allows us to optimise each component independently while maintaining overall system integrity. The approach provides conservative estimates for maximum bending moments and stresses, deflections, stability margins, and foundation reaction forces. It clearly establishes how wind loads travel from the panel surface through the structural system to the foundation and identifies potential failure mechanisms, including bending failure at the mast base, buckling instability of the slender mast, and foundation overturning. The methodology forms the foundation for more advanced dynamic and aeroelastic analyses by establishing the quasi-static baseline behaviour of the system.

In addition to the bending failure mode considered above, a slender cantilever mast can in principle fail by flexural-compressive buckling of the leeward fibre. For the configurations of practical interest in the present study, two features make this mode non-governing relative to root bending. First, on an inclined panel with $\theta < 45°$, the axial wind reaction at the mast head is dominated by the lift component (directed upward, placing the mast in tension), and the residual downward component is at most a few percent of the lateral drag, so the compressive axial stress at the root is small compared with the bending stress quantified above. Second, the geometrical proportions adopted in the numerical examples ($\gamma_m = h/t_m = 40$ with a steel mast) place the cross-section well below the slenderness limit at which Euler buckling would govern under the small axial load involved. For taller or more slender masts (say $\gamma_m > 80$), or for masts subjected to substantial deck-load such as in canopy-mounted PV systems, a separate flexural-compressive buckling check using AISC or Eurocode 3 provisions should be performed in addition to the analytical bending check developed here.

Figure 4 presents the structural response of a cantilevered solar panel mast subjected to horizontal wind loading. The results are based on the pseudo-static analysis framework developed in Section 3.1 and depict the variation of maximum bending stress $\sigma_{\max}$, tip deflection δ_m, and tip rotation θ_m with respect to wind velocity V, ranging from 0 to 80 m/s. The plots are generated using the following geometric and material parameters: mast thickness $t_m = 0.05$ m, mast height $h = 2.0$ m, panel width $b = 2.5$ m, mast width ratio $\epsilon = 0.03$, panel spans $l_1 = 2.0$ m, $l_2 = 1.0$ m, inclination angle $\theta = 30°$, Young's modulus $E = 210$ GPa, air density $\rho = 1.225$ kg/m^3, and pressure coefficients $C_p(30°) = 0.7$, $C_p(90°) = 1.28$.

The first subplot in **Figure 4** illustrates the variation in the maximum bending stress $\sigma_{\max}$ at the base of the mast as a function of wind speed. This stress is derived from **Equation (7)**, which includes contributions from the bending moment due to the aerodynamic force acting on the panel and the distributed wind pressure on the mast. The stress increases quadratically with wind velocity, in accordance with the dependence on dynamic pressure ρV^2. A horizontal reference line indicating the yield strength $\sigma_{y,m} = 250$ MPa of the structural steel mast is included to identify the threshold wind speed at which material failure becomes probable.

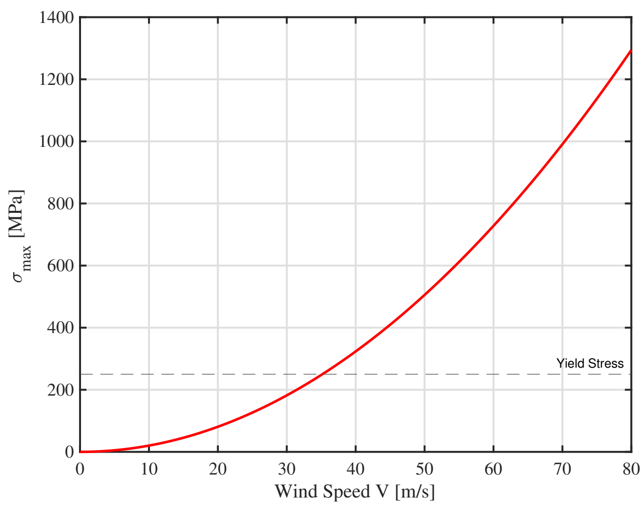

(a) Maximum stress vs. wind speed.

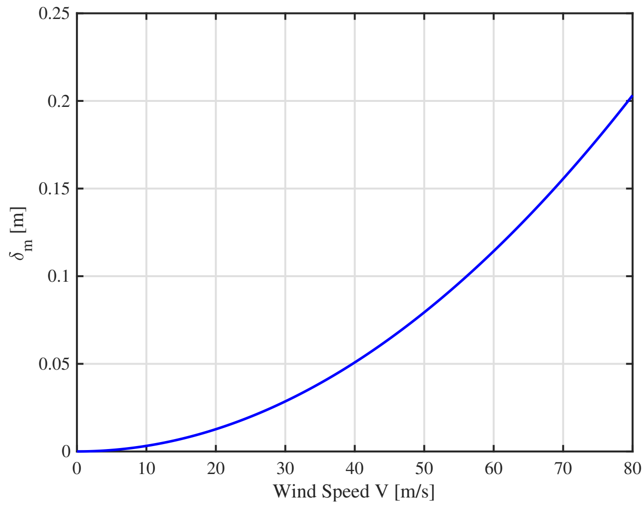

(b) Tip deflection vs. wind speed.

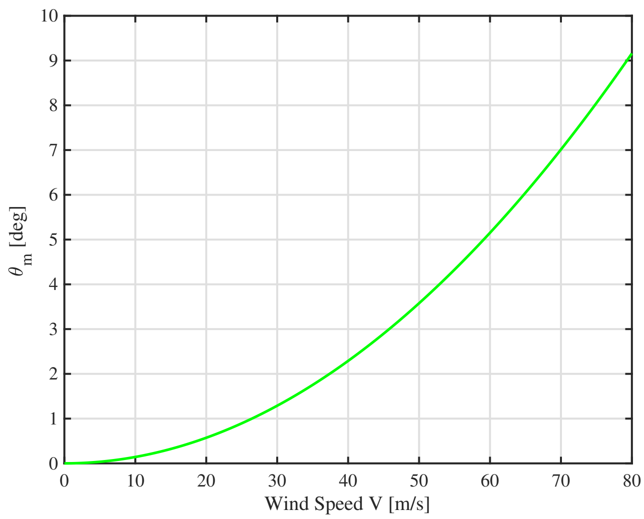

(c) Tip rotation vs. wind speed.

Figure 4. Structural response of a solar panel mast under horizontal wind loading: (**a**) maximum bending stress σ_{max}, (**b**) tip deflection δ_m, and (**c**) tip rotation θ_m as functions of wind speed V. The mast is $h = 2.0$ m tall and $t_m = 0.05$ m thick, with an inclined panel of width $b = 2.5$ m, overhangs $l_1 = 2.0$ m, $l_2 = 1.0$ m, and inclination angle $\theta = 30°$. The mast width is ϵb with $\epsilon = 0.03$. Material and fluid properties are $E = 210$ GPa, $\rho = 1.225\,\text{kg/m}^3$, $C_p(30°) = 0.7$, and $C_p(90°) = 1.28$.

The second subplot shows the corresponding mast tip deflection δ_m, derived using **Equation (13)**. This deflection aggregates the elastic contributions from the point force P, the transmitted moment M, and the distributed load q, each scaled appropriately with the mast geometry and material stiffness. The trend of the deflection curve reflects a combination of cubic and quartic growth in wind speed due to geometric amplification through the non-dimensional parameter $\gamma_m = h/t_m$. The plot underscores the role of mast slenderness and panel asymmetry in amplifying structural displacement.

The third subplot displays the tip rotation θ_m of the mast, computed using **Equation (15)**. This quantity is particularly relevant in determining the effective inclination angle of the solar panel, which becomes $\alpha = \theta + \theta_m$. The rotation increases non-linearly with wind speed and is expressed in degrees for physical interpretability.

 10.20935/AcadEnergy8386

Collectively, the three plots in **Figure 4** offer a comprehensive picture of the mast's structural performance under wind loading, forming a baseline for subsequent dynamic and aeroelastic analyses.

3.1.2. Failure analysis of the panel

In **Figure 5**, we show the wind loading on the solar panel only. The solar panel is, in general, a thinner structure and may be vulnerable to high wind speeds.

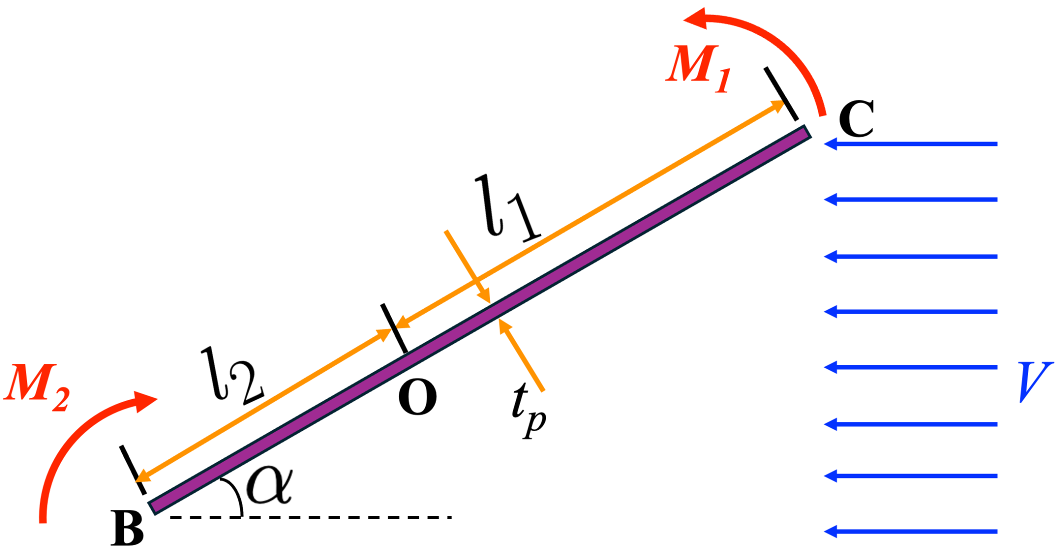

Figure 5. Wind loading (denoted by velocity V) on the solar panel only. The length of the panel is $l = l_1 + l_2$, the width is b, and the thickness is t_p. Two moments (denoted by M_1 and M_2) arise on the pivot point O, arising from wind pressures on lengths l_1 and l_2. The effective inclination angle is α, which is, in general, slightly more than the actual angle θ. This is due to the rotation of the mast.

The aerodynamic analysis in this section employs lift and drag coefficients rather than the pressure coefficients used in Section 3.1.1, reflecting different levels of analysis complexity required for each component. For the support column failure analysis in Section 3.1.1, simplified pressure coefficients provide adequate accuracy for preliminary force estimation and structural sizing, as the mast experiences primarily drag-dominated loading. However, the panel analysis requires consideration of both normal and tangential force components that arise from the complex pressure distribution over an inclined surface, necessitating the more comprehensive lift and drag coefficient approach.

The effective inclination angle is α, which is, in general, slightly more than the actual angle θ. This is due to the rotation of the mast. The rotation of the mast can be obtained from the forces and moments identified in the last section. The total rotation of the pivot point can be calculated by adding the rotation arising from the mast as

$$\alpha = \theta + \theta_m \tag{20}$$

This rotation relationship is derived from kinematic compatibility at the connection point O. For small deformations, the mast rotation θ_m is calculated using classical beam theory in **Equation (19)**, representing the slope of the deflected mast centreline at its free end. This approach is standard in structural analysis, where rigid connections transfer both forces and moments between components. This relationship is fundamental to capturing the coupling between mast flexibility and panel aerodynamics, representing a key advancement over analyses that assume rigid supports.

In aerodynamic analysis, the total force on an inclined surface subjected to wind flow can be decomposed into two orthogonal components:

- The drag force D, acting in the direction of the incoming freestream velocity;
- The lift force L, acting perpendicular to the freestream direction.

The lift and drag coefficients, denoted as $C_L(\alpha)$ and $C_D(\alpha)$, are dimensionless parameters that quantify the aerodynamic forces acting on a body immersed in a fluid flow. These coefficients are functions of the inclination angle α, Reynolds number, surface roughness, and geometry of the body [35, 38]. The drag coefficient $C_D(\alpha)$ represents the component of aerodynamic force acting in the direction of the freestream flow, typically caused by pressure differentials and skin friction. The lift coefficient $C_L(\alpha)$, on the other hand, quantifies the force component acting perpendicular to the flow direction, which arises due to asymmetrical pressure distribution around the body. For flat plates and panel-like structures, empirical approximations are often used to estimate these coefficients based on wind tunnel data or simplified potential flow theory [34, 39]. In particular, for thin flat plates at moderate Reynolds numbers, the drag coefficient is frequently approximated as $C_D(\alpha) \approx 1.28\cos(\alpha)$, while the lift coefficient can be represented as $C_L(\alpha) \approx 2\pi\sin(\alpha)\cos(\alpha)$, under the assumption of attached flow. The lift and drag coefficient expressions used here are derived from potential flow theory and are valid only under attached flow conditions, typically occurring at inclination angles below approximately $15°-20°$. For solar panels operating at steeper angles of $20°-45°$, flow separation and stall phenomena may become significant. The framework is therefore most appropriate for preliminary analysis of solar panels at moderate inclination angles, with the understanding that higher-angle installations require more sophisticated aerodynamic modelling approaches. These expressions in turn can be used in structural wind loading models, allowing the total aerodynamic force to be decomposed into components aligned with and normal to the surface of inclined panels. These forces per unit area are given by:

$$D = \frac{1}{2}\rho V^2 C_D(\alpha), \quad L = \frac{1}{2}\rho V^2 C_L(\alpha), \tag{21}$$

$$p_n = D\cos(\alpha) + L\sin(\alpha). \tag{22}$$

The lift and drag coefficient expressions are derived from classical flat plate theory under attached flow conditions [34, 35]. These formulations are valid for moderate angles of attack (typically $\alpha \lesssim 20°$) where flow separation is minimal. This is the same validity limit stated in Section 3.1.2; the apparent inconsistency in earlier drafts has been removed. The results presented in this manuscript at $\theta = 30°$ and $\theta = 45°$ should therefore be interpreted as analytical extrapolations that expose the parametric sensitivity of the closed-form expressions, rather than as quantitative predictions of the absolute critical wind speed at those angles. The lift coefficient expression follows from thin airfoil theory, with the $\sin(\alpha)\cos(\alpha)$ dependence representing the projection of circulation-induced forces. The drag coefficient incorporates both pressure drag and friction effects, with the 1.28 factor representing the typical drag coefficient for a flat plate in cross-flow. Substituting the expressions for D and L, we obtain:

$$p_n = \frac{1}{2}\rho V^2 \left[C_D(\alpha)\cos(\alpha) + C_L(\alpha)\sin(\alpha)\right]. \tag{23}$$

This expression accounts for the full aerodynamic force acting perpendicular to the inclined panel, capturing both the pressure drag and lift-induced effects. These aerodynamic relationships are most accurate for attached flow conditions at moderate inclination angles. For higher angles where flow separation occurs, empirical corrections or computational fluid dynamics analysis may be required for precise force prediction, though the analytical framework provides reasonable estimates for preliminary design assessment. The relative contribution of the two terms depends on the inclination angle α and the aerodynamic behaviour of the panel (i.e., whether it behaves like a flat plate, an aerofoil, or a bluff body). Here, we consider that the panel acts like a flat plate. The moments about the pivot point O arising due to force per unit area can be obtained as

$$M_i = \frac{(p_n b) l_i^2}{2}, \quad i = 1, 2 \tag{24}$$

The maximum stress arising due to these moments can be obtained as $\frac{M_i(t_p/2)}{I_p} = \frac{6M_i}{bt_p^2}$. Although the moment vectors associated with M_1 and M_2 are oppositely directed about O (one represents the bending about O of the segment OB, the other of the segment OC), the bending stresses they produce at the panel root act on the same panel fibre. The uniform pressure p_n pushes both cantilevered segments toward the leeward direction, so the leeward (downstream) face of the panel cross-section at O is in tension under both moments simultaneously, and the windward face is in compression under both. The maximum tensile fibre stress at the root therefore corresponds to the sum of the two individual maximum stresses, not their difference. Adding the stresses arising from both moments, we have

$$\sigma_{\text{max}} = \frac{6M_1}{bt_p^2} + \frac{6M_2}{bt_p^2} = \frac{3}{2}\rho V^2 \left[C_D(\alpha)\cos(\alpha) + C_L(\alpha)\sin(\alpha)\right]\left(\eta_{p_1}^2 + \eta_{p_2}^2\right) \tag{25}$$

Here, the non-dimensional structural parameters of the panel are

$$\eta_{p_1} = \frac{l_1}{t_p} \quad \text{and} \quad \eta_{p_2} = \frac{l_2}{t_p} \tag{26}$$

This formulation is particularly useful in structural analysis and aeroelastic modelling, as it allows for the calculation of resultant loads that directly influence bending moments, deflections, and stress distributions in inclined structural elements such as solar panels or facade systems [40].

In the context of aeroelastic failure analysis of cantilevered solar panels, a fragility curve represents the probability that the structure fails as a function of a controlling load parameter. For wind-induced failures, the controlling parameter is typically the wind velocity V, and failure is assumed to occur when the induced stress exceeds the yield stress of the material. Failure is assumed to occur when $\sigma_{\text{max}} \geq \sigma_y$, where σ_y is the yield stress of the material (e.g., 140 MPa for Aluminium 6061-T4). To model the probability of this event, we define a fragility function $P_f(V)$, which represents the probability that the wind velocity V leads to a stress exceeding σ_y. The lognormal form for the stress capacity adopted below follows the canonical multiplicative-error reliability model of Ellingwood, Galambos, MacGregor, and Cornell [41], which underpins the lognormal capacity assumption used throughout the LRFD code-calibration literature, and is the standard practice in the wind-induced damage/risk assessment community, including the FEMA Hazus hurricane technical manual [42] and the residential hurricane damage model of Pinelli et al. [43]. The dispersion value $\beta = 0.4$ adopted in the numerical examples is consistent with the values reported in those references for structural aluminium and steel yield capacities under fluctuating loads. Assuming lognormal uncertainty in the stress capacity, the fragility function takes the form:

$$P_f(V) = \Phi\left(\frac{\ln \sigma_{\text{max}}(V) - \ln \sigma_y}{\beta}\right), \tag{27}$$

where

- $\Phi(\cdot)$ is the standard normal cumulative distribution function;
- β is the lognormal standard deviation (dispersion);
- $\sigma_{\max}(V)$ is the deterministic stress as a function of wind velocity V;
- σ_y is the deterministic or median material yield stress.

Substituting the expression for $\sigma_{\max}(V)$, the fragility function becomes:

$$P_f(V) = \Phi\left(\frac{\ln\left[\frac{3}{2}\rho V^2 \left[C_D(\alpha)\cos(\alpha) + C_L(\alpha)\sin(\alpha)\right]\left(\eta_{p_1}^2 + \eta_{p_2}^2\right)\right] - \ln\sigma_y}{\beta}\right). \tag{28}$$

This expression defines the fragility curve as a function of wind velocity. It reflects the increasing probability of failure with increasing wind speed, moderated by the structural configuration (η_{p_1}, η_{p_2}), orientation (α), and material strength. The shape of the curve is also governed by the dispersion parameter β, which accounts for epistemic uncertainty in parameters such as material (e.g., Aluminium 6061-T4) properties, structural modelling, and aerodynamic coefficients. The fragility $P_f(V)$ defined here is the conditional probability $P(\text{failure} \mid V)$ of failure given a wind speed V. The unconditional probability of failure over the service life of an installation is obtained by convolving this conditional fragility with the appropriate wind hazard distribution, for example, the ASCE 7-22 basic wind speed contours, the Eurocode EN 1991-1-4 storm wind speeds, the Enhanced Fujita scale of McDonald and Mehta [44] for tornado intensity, or the FEMA Hazus hurricane intensity model [42]. This separation of the structural fragility from the climatic hazard is the standard framework in performance-based wind engineering [36]. The model can be used to evaluate critical wind speeds associated with specified failure probabilities or to integrate with risk assessment frameworks for wind-sensitive infrastructure.

Figure 6 illustrates the variation in maximum stress $\sigma_{\max}$ in solar panels as a function of wind velocity for three different panel configurations characterised by their non-dimensional parameters $\eta_{p1} = l_1/t_p$ and $\eta_{p2} = l_2/t_p$. The panel labels "Type I", "Type II", and "Type III" used in this subsection denote a local parametric sweep specific to the pseudo-static stress analysis, with the values of η_{p1} and η_{p2} given in the caption of **Figure 6**. The same labels are re-used in the divergence analysis (Section 3.2) and in the flutter analysis (Section 3.3) for a different parametric sweep tailored to each analysis; the numerical values associated with each label in those sections are stated separately and should not be carried over from one section to another.

The results demonstrate that larger panels with higher aspect ratios (Type III: $\eta_{p1} = 150$, $\eta_{p2} = 100$) experience significantly higher stress levels compared to smaller configurations (Type I: $\eta_{p1} = 100$, $\eta_{p2} = 50$), with the stress increasing quadratically with wind speed due to the ρV^2 dependence in the aerodynamic loading. The horizontal dashed line at 140 MPa represents the material yield stress threshold (for Aluminium 6061-T4), beyond which structural failure is anticipated. The corresponding fragility analysis presented in **Figure 7** translates these deterministic stress results into probabilistic failure assessments, revealing that larger panel configurations exhibit substantially higher failure probabilities at lower wind speeds. Reading the curves directly from **Figure 6**, at $V = 40$ m/s the maximum stress reaches approximately 100 MPa for the Type III panel and approximately 70 MPa for the Type I panel, both still below the 140 MPa yield threshold for Aluminium 6061-T4. The yield threshold is crossed first by the Type III panel near $V \approx 50$ m/s and by the Type I panel only beyond $V \approx 60$ m/s, after which the corresponding fragility curves in **Figure 7** climb steeply. This quantitative behaviour highlights the critical importance of panel sizing in wind-resistant design for solar installations.

Figure 8 demonstrates the pronounced influence of panel inclination angle on maximum stress development under wind loading for Type I panel configuration ($\eta_{p1} = 100$, $\eta_{p2} = 50$).

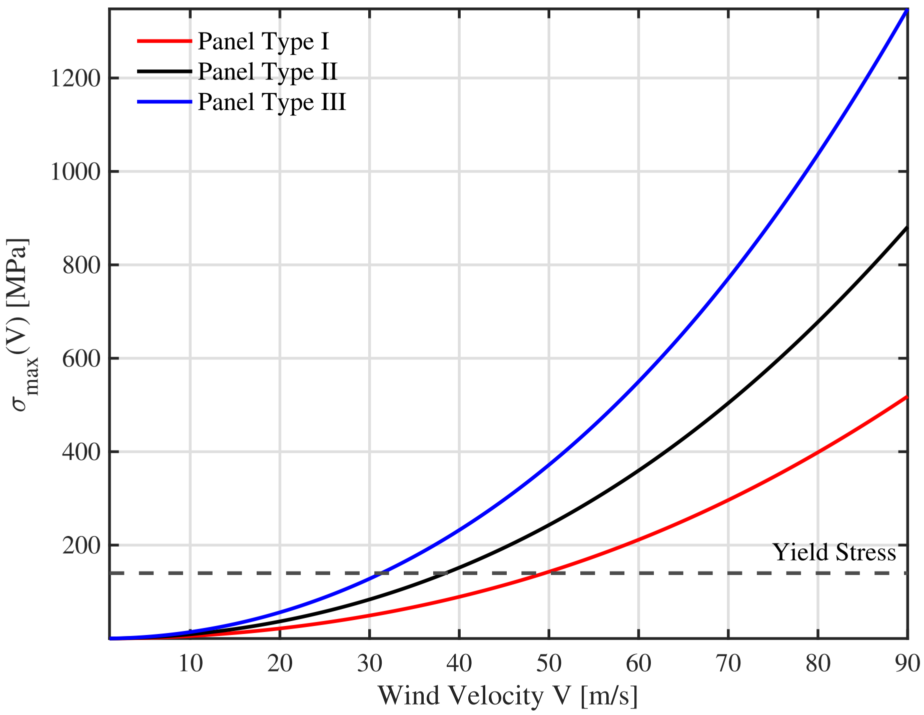

Figure 6. Maximum stress $\sigma_{\max}$ in solar panels as a function of wind velocity for three different panel configurations: Type I ($\eta_{p1} = 100$, $\eta_{p2} = 50$), Type II ($\eta_{p1} = 125$, $\eta_{p2} = 75$), and Type III ($\eta_{p1} = 150$, $\eta_{p2} = 100$). The horizontal dashed line indicates the material yield stress threshold.

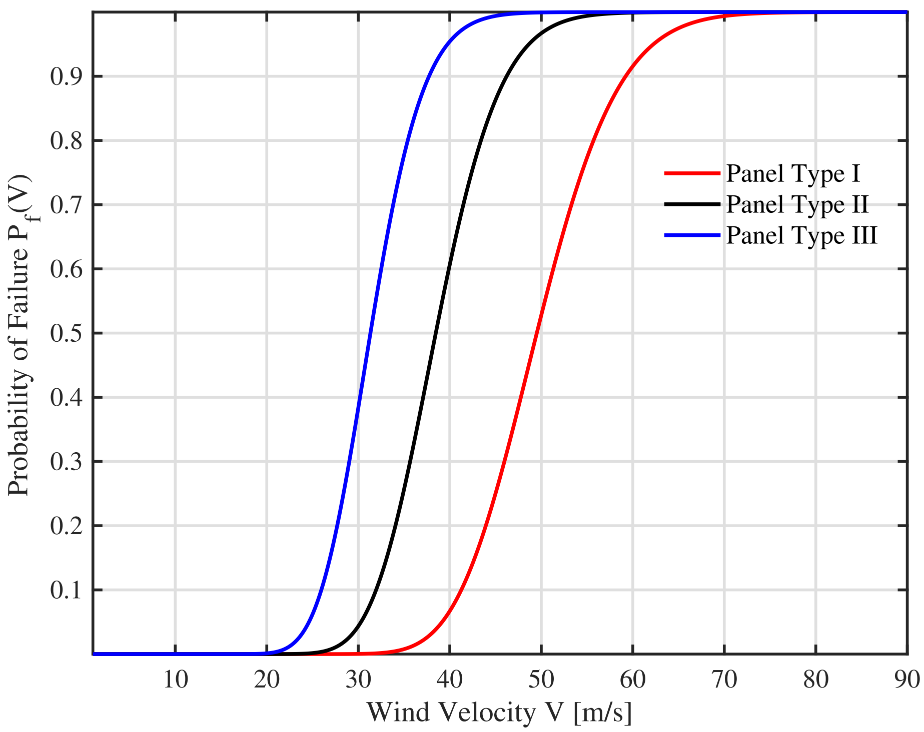

Figure 7. Fragility curves showing probability of failure $P_f(V)$ versus wind velocity for three panel configurations with inclination angle $\theta = 30°$. Larger panels (higher η_{p1}, η_{p2} values) exhibit higher failure probabilities at lower wind speeds.

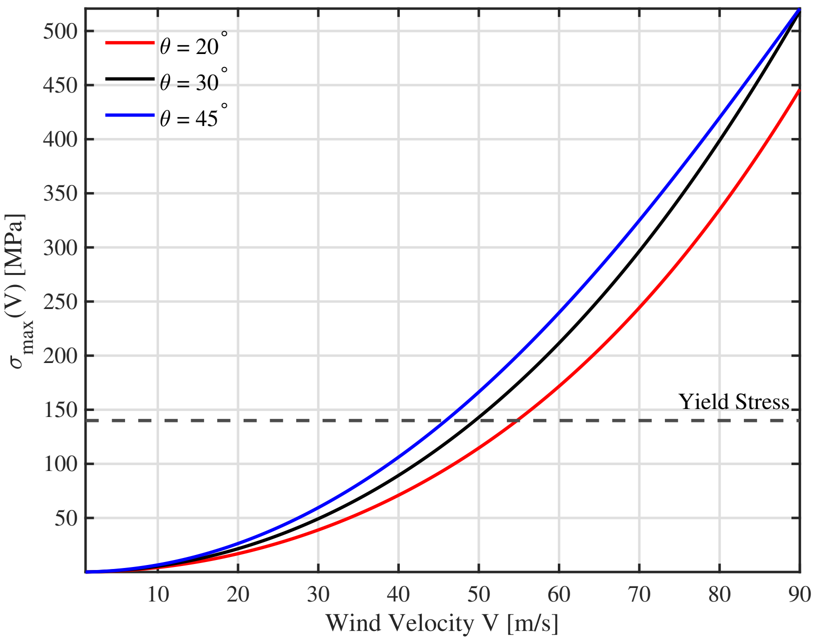

Figure 8. Maximum stress σ_{max} in solar panels versus wind velocity for different panel inclination angles ($\theta = 20°$, 30°, 45°) for Type I panels. Steeper inclination angles result in higher stress levels due to increased aerodynamic loading.

The results reveal that steeper inclination angles generate substantially higher stress levels, with the $\theta = 45°$ configuration producing approximately twice the stress magnitude compared to the $\theta = 20°$ case at equivalent wind velocities. This behaviour is attributed to the increased normal pressure component $p_n = \frac{1}{2}\rho V^2[C_D(\alpha)\cos(\alpha) + C_L(\alpha)\sin(\alpha)]$ acting on the inclined surface, where both drag and lift contributions intensify with larger inclination angles through the trigonometric dependencies and pressure coefficient variations. The corresponding probabilistic assessment in **Figure 9** quantifies this trend through fragility curves, showing that steeper panel orientations exhibit significantly earlier onset of failure probability, with the $\theta = 45°$ configuration reaching 50% failure probability at approximately 45 m/s compared to 65 m/s for the $\theta = 20°$ case. While results for Type II and Type III panel configurations are not presented here, the scaling relationships established in **Figure 6** and **Figure 7** indicate that these larger panel geometries would exhibit proportionally higher stress magnitudes and elevated failure probabilities across all inclination angles, thereby further constraining the operational wind speed envelope for steeper solar panel installations.

3.2. Static divergence analysis

Static divergence analysis examines the onset of aeroelastic instability when aerodynamic forces become sufficient to overcome structural restoring forces, leading to divergent behaviour without oscillatory motion. Unlike the pseudo-static analysis, which assumes equilibrium under steady loading, static divergence identifies the critical wind speed at which the system loses static stability due to aerodynamic–structural coupling. For solar panel arrays where multiple panels are connected together with adequate structural redundancy, mast lateral-torsional instability is typically not a governing concern due to the distributed support system. However, individual panel torsional divergence remains critical as each panel can experience local instability about its attachment points. The key parameter governing this behaviour is the torsional stiffness k_θ, which represents the elastic restoring moment per unit twist angle and depends on the panel's material properties, cross-sectional geometry, and boundary conditions. Next, we propose an approach to obtain the torsional stiffness k_θ.

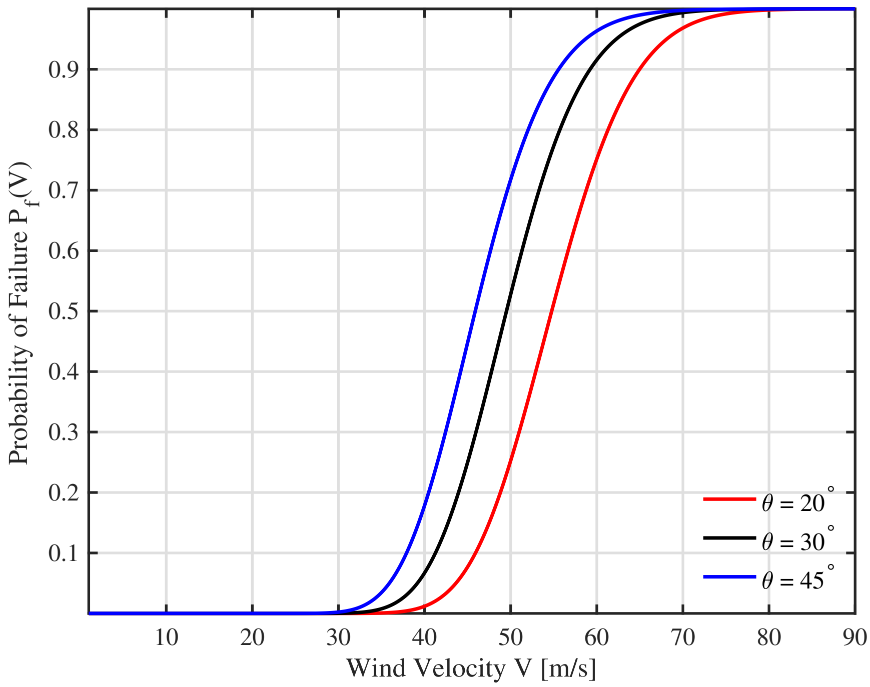

Figure 9. Fragility curves for different panels (for Panel Type I) inclination angles show how steeper orientations lead to earlier onset of failure probability. The curves demonstrate the significant influence of the panel tilt angle on structural reliability under wind loading.

3.2.1. Equivalent torsional stiffness of the solar panel

The magnitude of k_θ directly determines the critical divergence wind speed and thus establishes the operational limits for safe panel operation under aerodynamic loading. We derive the equivalent torsional stiffness of the solar panel by superimposing two mechanical cases: (1) the panel is rigid and the rotational stiffness of the mast at the pivot point O is considered, and (2) the mast is rigid, and we consider the effective rotation of the panel due to an applied moment. In **Figure 10**, the schematic diagram of the system is shown.

The panel in **Figure 10** is subjected to virtual force P at the two end points. This results in a virtual moment

$$M = Pl \tag{29}$$

The rotation of the mast ϕ_m due to this moment can be related to its rotational stiffness k_m as

$$M = \phi_m k_m, \quad \text{where} \quad k_m = \frac{EI_m}{h} \tag{30}$$

Now let us consider that the mast is rigid and obtain the rotation of the panel when point O is fixed. In this case, OC and OB become cantilevers with a fixed end at O. The deflections at points C and B are

$$\delta_B = \frac{Pl_1^3}{3EI_p} \quad \text{and} \quad \delta_C = \frac{Pl_2^3}{3EI_p} \tag{31}$$

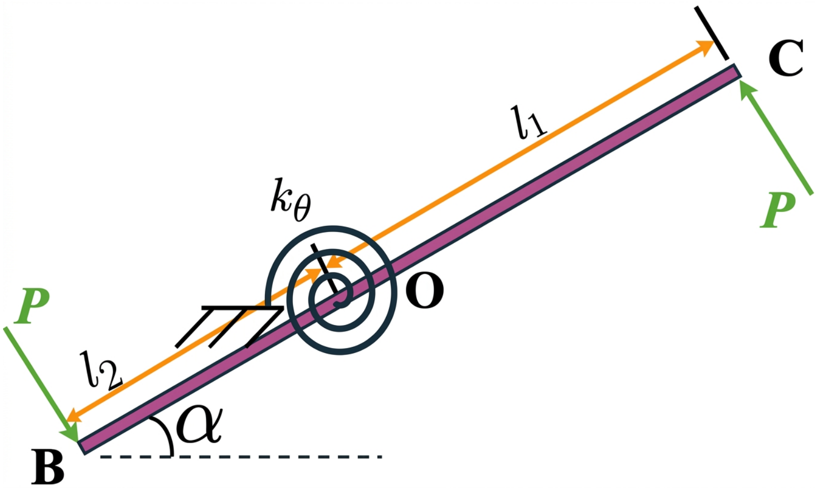

Figure 10. Torsional spring k_θ of the solar panel. A virtual force P is applied at the two ends to obtain the effective rotation of the coupled mast–panel model.

The total rotation of the panel BC about O is

$$\phi_p = \frac{\delta_B + \delta_C}{l} \tag{32}$$

The total rotation of the mast–panel system is obtained by adding the rotation of the mast at point O and the rotation of the panel as

$$\phi = \phi_m + \phi_p \tag{33}$$

Geometrically, ϕ_p is the rigid body rotation of the panel chord BC about the pivot O when the mast is held fixed there, induced by the cantilever bending of the two segments OB and OC under the virtual moment. The superposition $\phi = \phi_m + \phi_p$ follows from kinematic rotation compatibility at the rigidly framed connection at O: under a common applied moment, the panel chord rotates with the mast (through ϕ_m) and additionally relative to the mast (through ϕ_p). Both contributions are linear in the applied moment in the small-deformation regime, so the two compliances are added and the inverse of their sum is the equivalent torsional stiffness k_θ. This is the standard springs-in-series compliance argument and, within the assumed small-rotation, linear elastic framework, is mathematically equivalent to the coupled multi-body solution [40, 45]. The effective torsional stiffness k_θ of the system can be defined from the total virtual moment and rotation as

$$M = k_\theta \phi = k_\theta \left(\phi_m + \phi_p\right) = k_\theta \left(\frac{Mh}{EI_m} + \frac{1}{l}\left[\frac{Pl_1^3}{3EI_p} + \frac{Pl_2^3}{3EI_p}\right]\right) \tag{34}$$

Substituting $M = Pl$ and cancelling terms, we have

$$1 = k_\theta \left(\frac{h}{EI_m} + \frac{1}{l^2}\left[\frac{l_1^3}{3EI_p} + \frac{l_2^3}{3EI_p}\right]\right) = k_\theta \frac{1}{E}\left(\frac{12\gamma_m}{\epsilon b t_m^2} + \frac{4}{bl^2}\left[\eta_{p_1}^3 + \eta_{p_2}^3\right]\right) \tag{35}$$

Rearranging the terms on the left-hand side

$$1 = k_\theta \frac{4}{\epsilon E b l^2}\left(3\gamma_m \left[\eta_{p_1} + \eta_{p_2}\right]^2 + \epsilon\left[\eta_{p_1}^3 + \eta_{p_2}^3\right]\right) \tag{36}$$

$$\text{or} \quad k_\theta = \frac{\epsilon E b l^2}{4\Gamma} \quad \text{where} \quad \Gamma = 3\gamma_m \left[\eta_{p_1} + \eta_{p_2}\right]^2 + \epsilon\left[\eta_{p_1}^3 + \eta_{p_2}^3\right] \tag{37}$$

This rotational stiffness governs the overall torsional behaviour of the coupled mast–panel system. The rotational stiffness expression in the above equation represents the fundamental resistance of the coupled mast–panel system to torsional deformation and plays a critical role in determining the aeroelastic stability of solar panel installations. The term $k_\theta = \frac{\epsilon E b l^2}{4\Gamma}$ reveals that the torsional stiffness is directly proportional to the elastic modulus E and the panel width b, indicating that stiffer materials and wider panels provide greater resistance to twist. The quadratic dependence on the total panel length l demonstrates the significant geometric advantage of shorter panels in maintaining torsional rigidity. The dimensionless parameter $\Gamma = 3\gamma_m[\eta_{p_1} + \eta_{p_2}]^2 + \epsilon[\eta_{p_1}^3 + \eta_{p_2}^3]$ encapsulates the combined flexibility contributions from both the mast and panel components, where mast slenderness ($\gamma_m = h/t_m$) and panel geometry ratios ($\eta_{p_1} = l_1/t_p$, $\eta_{p_2} = l_2/t_p$) are additive rather than multiplicative. Physically, the first term $3\gamma_m[\eta_{p_1} + \eta_{p_2}]^2$ represents the mast's rotational flexibility scaled by the panel's moment arm, while the second term $\epsilon[\eta_{p_1}^3 + \eta_{p_2}^3]$ captures the panel's own bending compliance about the pivot point. The inverse relationship between k_θ and Γ indicates that both tall, slender masts and large, thin panels independently reduce the system's torsional stiffness, with their effects being cumulative in creating configurations most susceptible to divergence instabilities. This rotational stiffness directly determines the critical wind speed for torsional divergence, establishing the fundamental design trade-off between structural efficiency and aeroelastic stability in solar panel systems.

3.2.2. Panel torsional divergence analysis

The solar panel experiences torsional divergence when the aerodynamic moment about the pivot point O overcomes the panel's torsional stiffness k_θ. Building upon the aerodynamic force analysis from Section 3.2, the moment coefficient for a flat plate can be expressed as:

$$C_M(\alpha) = \frac{1}{4}[C_L(\alpha) - C_D(\alpha)\tan(\alpha)] \tag{38}$$

where the lift and drag coefficients follow the established relationships $C_L(\alpha) \approx 2\pi\sin(\alpha)\cos(\alpha)$ and $C_D(\alpha) \approx 1.28\cos(\alpha)$ [34, 35]. The total aerodynamic moment about point O due to the distributed pressure loading becomes:

$$M_{aero} = \frac{1}{2}\rho V^2 b \frac{(l_1 + l_2)^2}{2} C_M(\alpha) \tag{39}$$

The elastic restoring moment is provided by the panel's torsional stiffness, which for small twist angles ϕ, can be expressed as:

$$M_{elastic} = k_\theta \phi \tag{40}$$

where k_θ is the torsional stiffness that will be derived in subsequent analysis. Critical divergence occurs when the aerodynamic moment equals the maximum elastic restoring moment capacity. At the point of divergence, the rate of change of aerodynamic moment with respect to twist angle equals the torsional stiffness:

$$\frac{\partial M_{aero}}{\partial \phi} = k_\theta \tag{41}$$

Since the effective angle of attack changes with panel twist as $\alpha = \theta + \theta_m + \phi$, we have:

$$\frac{\partial M_{aero}}{\partial \phi} = \frac{1}{2}\rho V^2 b \frac{(l_1 + l_2)^2}{2} \frac{\partial C_M(\alpha)}{\partial \alpha} \tag{42}$$

The derivative of the moment coefficient with respect to the angle of attack is:

$$\frac{\partial C_M(\alpha)}{\partial \alpha} = \frac{1}{4}\left[\frac{\partial C_L(\alpha)}{\partial \alpha} - \frac{\partial C_D(\alpha)}{\partial \alpha}\tan(\alpha) - C_D(\alpha)\sec^2(\alpha)\right] \tag{43}$$

For the flat plate approximations, these derivatives become:

$$\frac{\partial C_L(\alpha)}{\partial \alpha} = 2\pi[\cos(2\alpha)], \quad \frac{\partial C_D(\alpha)}{\partial \alpha} = -1.28\sin(\alpha) \tag{44}$$

Using these, the derivative of the moment coefficient with respect to the angle of attack simplifies to:

$$\frac{\partial C_M(\alpha)}{\partial \alpha} = \frac{1}{2}\pi\cos(2\alpha) - 0.32\cos(\alpha) \tag{45}$$

The divergence analysis presented here inherits the aerodynamic modelling limitations discussed in Section 2.2, where the lift and drag coefficient expressions are valid only under attached flow conditions typically occurring at inclination angles below $15° - 20°$. For solar panels operating at steeper angles commonly used for optimal solar exposure ($20° - 45°$), flow separation and stall phenomena may invalidate these theoretical relationships, potentially leading to unconservative divergence velocity predictions. The analytical framework, therefore, provides reliable divergence estimates primarily for moderate-angle installations, while steeper configurations require empirical aerodynamic data or computational approaches that account for separated flow conditions. The analysis developed here should be applied with caution to practical solar installations, recognising that the theoretical aerodynamic predictions can become increasingly inaccurate as panel inclination angles exceed the attached flow regime.

Substituting the above expressions and setting the aerodynamic moment derivative equal to the torsional stiffness yields the critical divergence condition:

$$\frac{1}{2}\rho V_{div}^2 b \frac{(l_1 + l_2)^2}{2}\frac{\partial C_M(\alpha)}{\partial \alpha} = k_\theta \tag{46}$$

Solving for the divergence velocity:

$$V_{div} = \sqrt{\frac{4k_\theta}{\rho b l^2 \frac{\partial C_M(\alpha)}{\partial \alpha}}} \tag{47}$$

Substituting the expression of k_θ from the previous section, this can be simplified to

$$\begin{aligned} V_{div} &= \sqrt{\frac{4\frac{\epsilon E b l^2}{4\Gamma}}{\rho b l^2 \frac{\partial C_M(\alpha)}{\partial \alpha}}} = \sqrt{\frac{E}{\rho}\frac{\epsilon}{\Gamma\left[\frac{1}{2}\pi\cos(2\alpha) - 0.32\cos(\alpha)\right]}} \\ &= \sqrt{\frac{E}{\rho}\frac{\epsilon}{\left(3\gamma_m\left[\eta_{p_1} + \eta_{p_2}\right]^2 \epsilon\left[\eta_{p_1}^3 + \eta_{p_2}^3\right]\right)\left[\frac{1}{2}\pi\cos(2\alpha) - 0.32\cos(\alpha)\right]}} \end{aligned} \tag{48}$$

This divergence velocity expression represents the critical wind speed threshold beyond which the solar panel system becomes aeroelastically unstable, making it a fundamental design criterion for safe operation [38]. The expression

$$V_{div} = \sqrt{\frac{E}{\rho}}\sqrt{\frac{\epsilon}{3\gamma_m[\eta_{p_1} + \eta_{p_2}]^2 + \epsilon[\eta_{p_1}^3 + \eta_{p_2}^3]}}\sqrt{\frac{1}{\frac{1}{2}\pi\cos(2\alpha) - 0.32\cos(\alpha)}} \tag{49}$$

reveals several critical physical insights. The term $\sqrt{E/\rho}$ represents the characteristic velocity scale of elastic waves in the material, establishing the fundamental speed limit governed by material properties [46]. The geometric factor $\sqrt{\frac{\epsilon}{3\gamma_m[\eta_{p_1}+\eta_{p_2}]^2+\epsilon[\eta_{p_1}^3+\eta_{p_2}^3]}}$ demonstrates that divergence speed decreases with increasing mast slenderness (γ_m) and panel aspect ratios (η_{p_1}, η_{p_2}), reflecting the destabilizing effect of structural flexibility. The aerodynamic term $\sqrt{\frac{1}{\frac{1}{2}\pi\cos(2\alpha)-0.32\cos(\alpha)}}$ captures the dependence on panel inclination angle α. The two contributions in the denominator vary with α in the same sense but at very different rates: $\frac{1}{2}\pi\cos(2\alpha)$ decreases from $\pi/2$ at $\alpha = 0$ to zero at $\alpha = 45°$, while $0.32\cos(\alpha)$ decreases only modestly from 0.32 to 0.226 over the same range. The first term therefore dominates the variation, and the net derivative $\partial C_M/\partial\alpha$ decreases monotonically with α throughout the range of practical interest. The divergence velocity V_{div}, which scales as $1/\sqrt{\partial C_M/\partial\alpha}$, correspondingly increases with the inclination angle in this range. Beyond $\alpha \approx 45°$ the derivative changes sign and the present analysis no longer predicts torsional divergence; in that regime, the instability becomes stall-driven and lies outside the scope of the attached flow aerodynamic model used here. The expression provides a direct analytical tool to assess the trade-offs between structural efficiency (minimising material through slender designs) and aeroelastic stability (maintaining adequate stiffness), enabling optimal design of wind-resistant solar panel installations [39].

While **Equation (48)** formally requires the effective inclination angle $\alpha = \theta + \theta_m$ for rigorous application, the velocity-dependent nature of the mast rotation θ_m creates an implicit relationship that complicates direct solution of the divergence velocity. For practical implementation, the initial approximation $\alpha \approx \theta$ provides a reasonable starting point for the analysis, particularly at moderate wind speeds where the mast rotation remains small compared to the geometric panel inclination. This approximation is physically justified because the mast rotation θ_m scales quadratically with wind velocity according to **Equation (19)**, while typical solar panel inclination angles range from $20°$ to $45°$, meaning that for wind speeds well below the divergence threshold, θ_m represents only a small perturbation to the dominant geometric angle θ. Furthermore, **Equation (48)** can be implemented iteratively to achieve convergent results: an initial divergence velocity estimate $V_{div}^{(0)}$ obtained using $\alpha^{(0)} = \theta$ can be used to calculate the corresponding mast rotation $\theta_m^{(1)}$ from **Equation (19)**, yielding an updated effective angle $\alpha^{(1)} = \theta + \theta_m^{(1)}$ for subsequent refinement of the divergence velocity prediction. This iterative approach typically converges rapidly due to the relatively weak coupling between mast deformation and aerodynamic moment coefficients for small angular perturbations, and the convergence criterion $|\alpha^{(n+1)} - \alpha^{(n)}| < \varepsilon$ ensures that the final divergence velocity accounts for the complete aeroelastic feedback while maintaining computational tractability for design applications.

In the context of wind-induced aeroelastic phenomena, torsional divergence represents a critical failure mode for cantilevered solar panels. Unlike material yielding or excessive deflection discussed before, divergence is a global instability triggered when aerodynamic moments overcome the system's torsional stiffness. Since this instability leads to uncontrollable deformation, identifying the wind speed at which it occurs is essential for ensuring structural safety. However, due to uncertainties in system parameters and environmental conditions, a deterministic divergence velocity alone is insufficient. A probabilistic approach using a fragility curve offers a more comprehensive measure of the system's vulnerability to wind-induced instability.

The fragility curve quantifies the probability that wind-induced torsional instability occurs as a function of the incident wind velocity. Mathematically, this is expressed using a cumulative distribution function that models the uncertainty in the critical divergence threshold. Assuming the divergence velocity V_{div} follows a lognormal distribution due to epistemic variability in material properties, geometric parameters, and aerodynamic coefficients, the probability of failure at wind speed V is given by $P_f(V) = \Phi\left(\frac{\ln V - \ln V_{\text{div}}}{\beta}\right)$, where $\Phi(\cdot)$ denotes the standard normal cumulative distribution function and β is the logarithmic standard deviation (dispersion). This statistical representation reflects the stochastic nature of aeroelastic failure and allows for a probabilistic interpretation of structural performance under uncertain wind loading. The fragility function provides a continuous transition from safe to failure states and is particularly suitable for reliability-based design and risk assessment of wind-sensitive solar panel systems.

Figure 11 presents the probabilistic assessment of torsional divergence failure through fragility curves that quantify the probability of aeroelastic instability as a function of wind velocity for three distinct panel configurations characterised by their non-dimensional geometric parameters.

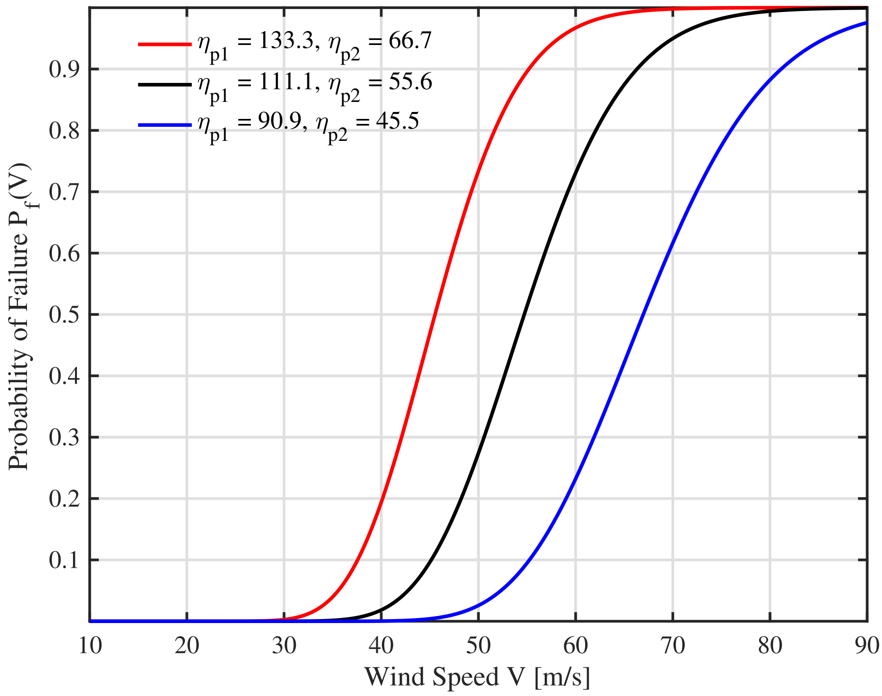

Figure 11. Divergence velocity fragility curves showing probability of aeroelastic failure $P_f(V)$ versus wind velocity for three panel configurations with inclination angle $\theta = 30°$: Panel Type I ($\eta_{p1} = 133.3$, $\eta_{p2} = 66.7$), Panel Type II ($\eta_{p1} = 111.1$, $\eta_{p2} = 55.6$), and Panel Type III ($\eta_{p1} = 90.9$, $\eta_{p2} = 45.5$). More slender panels (lower η_{p1}, η_{p2} values corresponding to thinner panels) exhibit substantially higher failure probabilities at lower wind speeds, with Panel Type III reaching 50% failure probability at approximately 32 m/s compared to 42 m/s for Panel Type I, demonstrating the critical influence of panel thickness on aeroelastic stability.

We note that the labels "Panel Type I/II/III" used in the divergence analysis here denote a local parametric sweep specific to this section, with η_{p1}, η_{p2} values that differ deliberately from those used in the pseudo-static stress analysis of Section 3.2 of Section 3 and from those used in the flutter analysis of Section 3.3 of Section 3; in each case, the relevant numerical values are stated explicitly in the figure caption or table immediately below. The analysis reveals that Panel Type I ($\eta_{p1} = 133.3$, $\eta_{p2} = 66.7$), $E = 210$ GPa, exhibits the most conservative failure behaviour, with the probability of divergence remaining below 10% for wind speeds up to approximately 35 m/s and reaching 50% failure probability at roughly 42 m/s. In contrast, the intermediate configuration Panel Type II ($\eta_{p1} = 111.1$, $\eta_{p2} = 55.6$) demonstrates moderately elevated vulnerability with 50% failure probability occurring at approximately 37 m/s, while the most slender Panel Type III ($\eta_{p1} = 90.9$, $\eta_{p2} = 45.5$) exhibits significantly compromised stability with 50% failure probability at only 32 m/s wind velocity. The systematic shift in fragility curves toward lower wind speeds with decreasing panel thickness demonstrates the profound influence of structural slenderness on aeroelastic stability, consistent with the inverse relationship between panel aspect ratios and divergence velocity established in **Equation (48)**. **Figure 12** complements this geometric analysis by examining the influence of the panel inclination angle on divergence fragility for a fixed Panel Type I configuration ($\eta_{p1} = 133.33$, $\eta_{p2} = 66.66$), revealing that steeper panel orientations substantially compromise aeroelastic stability through enhanced aerodynamic coupling.

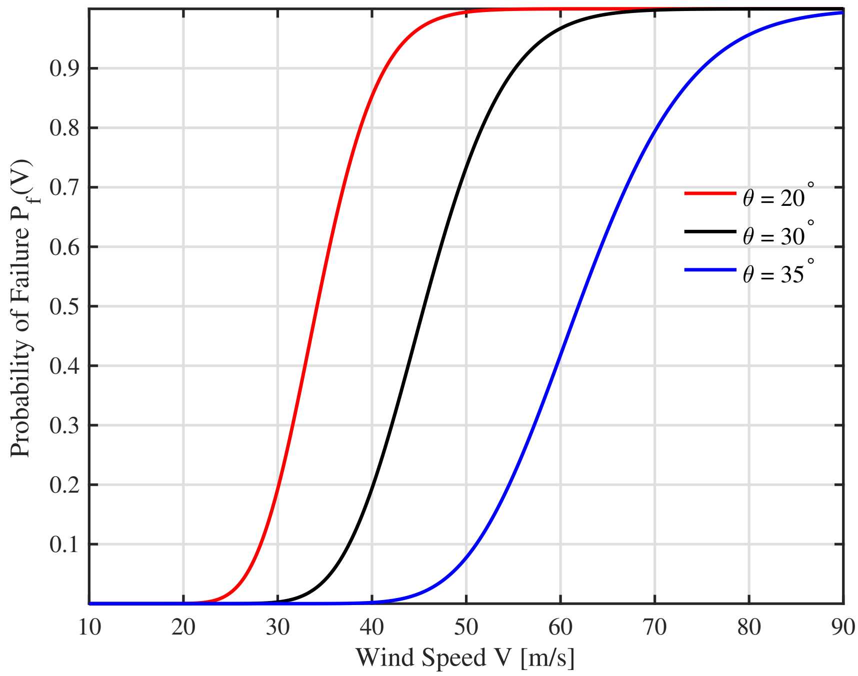

Figure 12. Divergence velocity fragility curves showing probability of aeroelastic failure $P_f(V)$ versus wind velocity for Panel Type I ($\eta_{p1} = 133.33$, $\eta_{p2} = 66.66$) at different inclination angles ($\theta = 20°, 30°, 35°$). Reading the curves directly from the figure, steeper panel orientations exhibit higher critical wind speeds for torsional divergence: the $\theta = 35°$ configuration reaches 50% failure probability at approximately 61 m/s, the $\theta = 30°$ configuration at approximately 47 m/s, and the shallowest $\theta = 20°$ configuration at approximately 35 m/s. This trend, opposite to that of the static stress fragility in Section 3.2 of Section 3, follows from the monotonic decrease in the aerodynamic moment coefficient derivative $\partial C_M/\partial\alpha$ with the inclination angle in the attached flow regime; the underlying mechanism is discussed in the text following this figure.

The results demonstrate that, reading the curves directly from **Figure 12**, the steeper $\theta = 35°$ orientation crosses the 50% failure probability at approximately $V \approx 61$ m/s, the $\theta = 30°$ configuration crosses 50% at a lower wind speed, and the shallowest $\theta = 20°$ orientation crosses 50% at the lowest wind speed of the three. This dependence on θ is opposite to that observed in the panel-stress fragility of Section 3.1.2, where steeper inclinations fail earlier. The reversal is a direct consequence of the angular dependence of the aerodynamic moment coefficient derivative

$$\frac{\partial C_M(\alpha)}{\partial \alpha} = \frac{1}{2}\pi\cos(2\alpha) - 0.32\cos(\alpha),$$

which decreases monotonically with α in the regime of practical interest. Since V_{div} scales as $1/\sqrt{\partial C_M/\partial\alpha}$, the divergence velocity therefore increases with the inclination angle. Physically, as the panel becomes steeper, the aerodynamic moment becomes less sensitive to a small twist perturbation, so the destabilising aerodynamic moment requires a higher wind speed to overcome the elastic restoring moment. This counter-intuitive trend, which is opposite to that of the static stress fragility, is one of the more useful analytical findings of the present study and highlights the fact that the static stress and divergence failure modes impose qualitatively different design constraints. Above $\alpha \approx 45°$ the derivative changes sign and torsional divergence in the present sense no longer occurs; in that regime, the relevant instability becomes stall-driven and lies outside the scope of the attached flow aerodynamic model used here. While results for Panel Types II and III are not presented in **Figure 12**, the scaling relationships established in **Figure 11** indicate that more slender configurations exhibit proportionally lower divergence velocities at any given θ, so that the more demanding combination from a divergence standpoint is the shallow-angle, thin-panel installation, complementing the static stress conclusion that the steeper-angle, larger-panel combination is the more demanding case for material yielding.

3.3. Simplified dynamic flutter analysis

Dynamic flutter analysis examines the onset of aeroelastic instability through oscillatory motion, where aerodynamic forces couple with structural dynamics to produce self-excited vibrations [35]. Unlike static divergence, which represents monotonic instability under steady loading, flutter manifests as sustained oscillations that grow in amplitude when the wind speed exceeds a critical threshold [38]. This phenomenon occurs when the aerodynamic energy input to the system exceeds the structural damping capacity, leading to exponentially growing oscillations that ultimately result in structural failure. For solar panel systems, torsional flutter represents the most critical dynamic instability mode, as the panels are particularly susceptible to pitching oscillations about their mounting points due to their large aspect ratios and relatively low torsional stiffness [39].

Here, we develop a simplified single-degree-of-freedom flutter model for torsional instability. Considering $\phi(t)$ as the dynamic rotation of the panel about the pivot point O, the equation of motion of the undamped panel is given by

$$J_p\ddot{\phi}(t) + k_\theta\phi(t) = M(t) \tag{50}$$

Here, J_p is the mass moment of inertia of the panel about the pivot point O, k_θ is the torsional stiffness derived in Section 3.2, and $M(t)$ is the time-dependent aerodynamic pitching moment. This fundamental equation represents the balance between inertial forces, elastic restoring forces, and aerodynamic excitation, forming the basis for understanding the dynamic behaviour of the solar panel system under oscillatory wind loading [34].

Structural damping is deliberately omitted from **Equation (50)**, so that the predicted flutter wind speeds derived below are lower-bound, conservative estimates of the true flutter onset. Including a small structural damping ratio ζ_s (typically 1–2% for welded aluminium-frame structures [47]) shifts the predicted onset upward in proportion to ζ_s. The undamped case adopted here is the standard worst-case design assumption in aeroelastic stability analysis [35, 48].

3.3.1. System dynamics and aerodynamic modelling

The accurate prediction of flutter requires careful modelling of both the structural dynamic properties and the unsteady aerodynamic forces. The structural dynamics are characterised by the mass moment of inertia and torsional stiffness, while the aerodynamic forces must account for the unsteady nature of the flow field around an oscillating panel. This coupling between structural motion and aerodynamic response creates a feedback mechanism that can either stabilise or destabilise the system, depending on the wind speed and system parameters.

The mass moment of inertia of the solar panel about the pivot point O must account for the distributed mass of both panel segments extending in opposite directions from the mounting point. This calculation is fundamental to determining the natural frequency of the system and the critical flutter speed. For a panel with uniform mass distribution, the moment of inertia about point O is calculated by considering the contributions from both segments l_1 and l_2, where the mass distribution affects the dynamic response characteristics significantly.

For segment OC (length l_1), the mass moment of inertia is calculated by integrating the second moment of the distributed mass:

$$J_{p1} = \int_0^{l_1} \rho_p b t_p x^2 dx = \frac{\rho_p b t_p l_1^3}{3} \tag{51}$$

Similarly, for segment BO (length l_2):

$$J_{p2} = \int_0^{l_2} \rho_p b t_p x^2 dx = \frac{\rho_p b t_p l_2^3}{3} \tag{52}$$

The total mass moment of inertia is obtained by summing the contributions from both segments:

$$J_p = J_{p1} + J_{p2} = \frac{\rho_p b t_p}{3}(l_1^3 + l_2^3) \tag{53}$$

where ρ_p is the material density of the panel, typically 2700 kg/m^3 for aluminium panels or 2500 kg/m^3 for glass–aluminium composite panels. This expression can be written in non-dimensional form using the previously defined geometric parameters:

$$J_p = \frac{\rho_p b t_p^4}{3}(\eta_{p1}^3 + \eta_{p2}^3) \tag{54}$$

where $\eta_{p1} = l_1/t_p$ and $\eta_{p2} = l_2/t_p$ are the non-dimensional panel aspect ratios. This formulation reveals that the moment of inertia scales with the fourth power of panel thickness and the cube of the panel lengths, highlighting the strong influence of panel geometry on dynamic characteristics.

For dynamic flutter analysis, the aerodynamic moment must account for unsteady effects arising from the panel's oscillatory motion. These unsteady effects are fundamentally different from the quasi-steady loading considered in static analysis, as they involve complex flow phenomena including shed vorticity, circulation changes, and added mass effects [49]. The total aerodynamic moment acting on an oscillating panel consists of steady and unsteady components:

$$M(t) = M_{steady}(\alpha) + M_{unsteady}(\dot{\phi}, \ddot{\phi}) \tag{55}$$

The steady component represents the mean aerodynamic loading and is identical to that used in static divergence analysis:

$$M_{steady}(\alpha) = \frac{1}{2}\rho V^2 b \frac{(l_1 + l_2)^2}{2} C_M(\alpha) \tag{56}$$

where $C_M(\alpha)$ is the moment coefficient derived previously. This steady component provides the baseline aerodynamic loading around which dynamic perturbations occur.

The unsteady component arises from the shed vorticity and added mass effects due to the panel's rotational motion. When a panel undergoes pitching oscillations, it generates a complex unsteady flow field characterised by vortex shedding from the panel edges and time-varying circulation around the panel. For a flat plate undergoing pitching oscillations, Theodorsen's classical unsteady aerodynamic theory provides the theoretical foundation for these effects. However, for engineering applications involving moderate-frequency oscillations, a simplified quasi-steady approach with added mass and damping terms is often sufficient and computationally more tractable [50]:

$$M_{unsteady} = -\rho V b \frac{(l_1 + l_2)^2}{2} C_{M_{\dot{\phi}}} \dot{\phi} - \rho b \frac{(l_1 + l_2)^3}{8} C_{M_{\ddot{\phi}}} \ddot{\phi} \tag{57}$$

where $C_{M_{\dot{\phi}}}$ and $C_{M_{\ddot{\phi}}}$ are aerodynamic derivatives representing aerodynamic damping and added mass effects, respectively. The first term represents aerodynamic damping, which can be either positive (stabilising) or negative (destabilising) depending on the flow conditions and panel geometry [51]. The second term represents the added mass effect, which effectively modifies the apparent inertia of the system due to the acceleration of fluid around the oscillating panel.

For a flat plate with a moderate aspect ratio, these coefficients are derived from classical unsteady aerodynamic theory rather than empirical curve fitting. The aerodynamic damping and added mass coefficients can be approximated based on Theodorsen's unsteady aerodynamic theory for oscillating flat plates in the quasi-steady limit:

$$C_{M\dot{\phi}} = -\frac{\pi}{4} \quad \text{and} \quad C_{M\ddot{\phi}} = \frac{\pi}{8} \tag{58}$$

The negative value of $C_{M\dot{\phi}} = -\pi/4$ arises from the phase relationship between panel motion and aerodynamic forces, representing the aerodynamic damping that can become destabilising under certain conditions. This coefficient quantifies how the aerodynamic moment responds to the angular velocity of the panel, with the negative sign indicating that increasing rotational velocity can lead to destabilising aerodynamic moments. The added mass coefficient $C_{M\ddot{\phi}} = \pi/8$ represents the theoretical limit for thin flat plates and accounts for the fluid acceleration around the oscillating panel, effectively modifying the apparent inertia of the system.

These values are well-established in the aeroelastic literature and represent fundamental aerodynamic responses derived from potential flow theory for thin airfoils [34, 35]. The coefficients have been extensively validated through wind tunnel experiments and computational fluid dynamics studies for flat plate configurations similar to solar panels. While more sophisticated unsteady aerodynamic models exist that account for viscous effects and flow separation, the quasi-steady approach with these theoretical coefficients provides adequate accuracy for the preliminary design framework presented here.

The quasi-steady assumption underlying these coefficients is most accurate for oscillations at moderate frequencies and small amplitudes, conditions typically encountered at the onset of flutter instability. For higher frequency oscillations or large amplitude motions, more sophisticated unsteady aerodynamic analysis incorporating full Theodorsen function corrections would be required.

Substituting the complete unsteady aerodynamic model into the fundamental equation of motion yields:

$$J_p \ddot{\phi} + k_\theta \phi = \frac{1}{2} \rho V^2 b \frac{(l_1 + l_2)^2}{2} C_M(\alpha) - \rho V b \frac{(l_1 + l_2)^2}{2} C_{M_{\dot{\phi}}} \dot{\phi} - \rho b \frac{(l_1 + l_2)^3}{8} C_{M_{\ddot{\phi}}} \ddot{\phi} \tag{59}$$

Rearranging terms to collect all inertial, damping, and stiffness contributions:

$$\left(J_p + \rho b \frac{(l_1 + l_2)^3}{8} C_{M_{\ddot{\phi}}}\right) \ddot{\phi} + \rho V b \frac{(l_1 + l_2)^2}{2} C_{M_{\dot{\phi}}} \dot{\phi} + k_\theta \phi = \frac{1}{2} \rho V^2 b \frac{(l_1 + l_2)^2}{2} C_M(\alpha) \tag{60}$$

This can be written in standard second-order linear differential equation form [45]:

$$J_{eff} \ddot{\phi} + C_{aero} \dot{\phi} + K_{eff} \phi = M_{steady} \tag{61}$$

where the effective system parameters are defined as:

$$J_{eff} = J_p + \rho b \frac{(l_1 + l_2)^3}{8} C_{M_{\ddot{\phi}}} \quad \text{(effective moment of inertia)} \tag{62}$$

$$C_{aero} = \rho V b \frac{(l_1 + l_2)^2}{2} C_{M_{\dot{\phi}}} \quad \text{(aerodynamic damping)} \tag{63}$$

$$K_{eff} = k_\theta \quad \text{(effective stiffness)} \tag{64}$$

The effective moment of inertia J_{eff} includes both the structural inertia and the aerodynamic added mass effect, which typically increases the apparent inertia of the system [34]. The aerodynamic damping C_{aero} is proportional to wind speed and can be either positive or negative depending on the sign of $C_{M_{\dot{\phi}}}$. When this damping becomes negative and sufficiently large in magnitude, it can overcome any structural damping present in the system, leading to flutter instability.

3.3.2. Flutter stability analysis and critical speed derivation

Flutter analysis requires determining the conditions under which the system transitions from stable to unstable behaviour. This transition occurs when the total damping in the system (structural plus aerodynamic) becomes zero or negative, leading to sustained or growing oscillations [38]. The mathematical approach involves examining the characteristic equation of the system and determining the critical wind speed at which the system eigenvalues cross the imaginary axis, indicating the onset of instability.

For flutter analysis, we consider small perturbations about the equilibrium position and linearise the aerodynamic moment about the mean angle of attack. This linearisation is valid for small-amplitude oscillations, which represent the initial stages of flutter development [35]. Assuming harmonic motion of the form $\phi(t) = \phi_0 e^{i\omega t}$, where $\omega = \omega_r + i\omega_i$ is the complex frequency, we substitute this solution into the homogeneous form of the equation of motion.

The complex frequency ω encodes both the oscillation frequency (ω_r) and the growth or decay rate (ω_i) of the motion [38]. For stable systems, $\omega_i < 0$, indicating exponential decay of disturbances. Neutral stability occurs when $\omega_i = 0$, corresponding to sustained oscillations, while instability manifests when $\omega_i > 0$, leading to exponentially growing oscillations.

Substituting the assumed harmonic solution into the linearised homogeneous equation:

$$J_{eff}(-\omega^2) + C_{aero}(i\omega) + K_{eff} - \frac{1}{2}\rho V^2 b \frac{(l_1 + l_2)^2}{2} \frac{\partial C_M}{\partial \alpha} = 0 \tag{65}$$

This yields the characteristic equation:

$$-J_{eff}\omega^2 + iC_{aero}\omega + K_{eff} - \frac{1}{2}\rho V^2 b \frac{(l_1 + l_2)^2}{2} \frac{\partial C_M}{\partial \alpha} = 0 \tag{66}$$

Expanding the complex frequency $\omega = \omega_r + i\omega_i$ and separating real and imaginary parts [45]: *Real part:*

$$-J_{eff}(\omega_r^2 - \omega_i^2) - C_{aero}\omega_r\omega_i + K_{eff} - \frac{1}{2}\rho V^2 b \frac{(l_1 + l_2)^2}{2} \frac{\partial C_M}{\partial \alpha} = 0 \tag{67}$$

Imaginary part:

$$-J_{eff}(2\omega_r\omega_i) + C_{aero}\omega_r = 0 \tag{68}$$

From the imaginary part equation, for non-trivial solutions where $\omega_r \neq 0$:

$$\omega_i = \frac{C_{aero}}{2J_{eff}} = \frac{\rho V b (l_1 + l_2)^2 C_{M_{\dot{\phi}}}}{4J_{eff}} \tag{69}$$

This expression reveals that the growth rate is directly proportional to the aerodynamic damping coefficient and wind speed, and inversely proportional to the effective moment of inertia. The critical insight is that when $C_{M_{\dot{\phi}}} < 0$ (as is typical for flat plates), increasing wind speed leads to increasingly negative aerodynamic damping, eventually causing the system to become unstable [52].

Flutter occurs when the system transitions from stable to neutrally stable behaviour, corresponding to the condition $\omega_i = 0$ with finite oscillation frequency $\omega_r \neq 0$. At this critical condition, the aerodynamic damping effects balance the structural damping, leading to sustained oscillations at the flutter frequency. From the imaginary part equation at flutter ($\omega_i = 0$), for non-trivial solutions where $\omega_r \neq 0$:

$$C_{aero} = 0 \tag{70}$$

This condition represents the balance between destabilising aerodynamic forces and structural restoring forces at a finite oscillation frequency.

The analysis focuses on determining the critical wind speed at which aeroelastic instability first occurs, which provides the most conservative design criterion for solar panel operations. For typical solar panel configurations, the effective moment of inertia is approximated as $J_{eff} \approx J_p$, neglecting aerodynamic added mass effects, which are small compared to structural inertia for the geometric ratios considered. For the critical flutter condition, we consider the onset of instability where the system transitions from stable to neutrally stable behaviour ($\omega_i = 0$). Using this approximation, the real part equation becomes:

$$-J_p \omega_r^2 + K_{eff} - \frac{1}{2}\rho V_{flutter}^2 b \frac{(l_1 + l_2)^2}{2} \frac{\partial C_M}{\partial \alpha} = 0 \tag{71}$$

The critical flutter speed is determined by the condition where the aerodynamic destabilising effect becomes sufficient to overcome the structural restoring forces. This occurs when the aerodynamic moment contribution equals the effective structural stiffness:

$$\frac{1}{2}\rho V_{flutter}^2 b \frac{(l_1 + l_2)^2}{2} \frac{\partial C_M}{\partial \alpha} = K_{eff} \tag{72}$$

Solving for the flutter speed, we have

$$V_{flutter} = \sqrt{\frac{2k_\theta}{\rho b (l_1 + l_2)^2 \frac{\partial C_M}{\partial \alpha}}} \tag{73}$$

This represents the minimum wind speed at which aeroelastic instability occurs. At this critical speed, the flutter frequency approaches zero ($\omega_r \to 0$), indicating that the instability manifests initially as a quasi-static divergence that can transition to dynamic flutter at higher wind speeds. This behaviour is characteristic of single-degree-of-freedom torsional systems where the flutter boundary coincides with the divergence condition. The derived flutter speed, therefore, represents the critical threshold for aeroelastic instability onset, providing a conservative estimate for safe operational wind limits.

Substituting the expression for k_θ from **Equation (37)** and the moment coefficient derivative from Section 3.2.2, we have

$$V_{flutter} = \sqrt{\frac{2 \cdot \frac{\epsilon E b l^2}{4\Gamma}}{\rho b l^2 \left[\frac{1}{2}\pi \cos(2\alpha) - 0.32\cos(\alpha)\right]}} \tag{74}$$

where $l = l_1 + l_2$ is the total panel length. Simplifying this expression, one obtains

$$V_{flutter} = \sqrt{\frac{E}{\rho}}\sqrt{\frac{\epsilon}{2\Gamma}}\frac{1}{\sqrt{\frac{1}{2}\pi \cos(2\alpha) - 0.32\cos(\alpha)}} \tag{75}$$

where $\Gamma = 3\gamma_m \left[\frac{\eta_{p1}+\eta_{p2}}{2}\right]^2 + \epsilon[\eta_{p1}^3 + \eta_{p2}^3]$ is the flexibility parameter derived previously.

The flutter speed expression in **Equation (75)** has a remarkably similar functional form to the divergence speed derived in **Equation (48)**, differing only in the leading coefficient. Specifically, the ratio of flutter to divergence speed is:

$$\frac{V_{flutter}}{V_{divergence}} = \sqrt{\frac{1}{2}} \approx 0.707 \tag{76}$$

This fundamental relationship indicates that *flutter occurs at approximately 70% of the divergence speed*, which is consistent with classical aeroelastic theory for single-degree-of-freedom torsional systems [38]. This result has profound implications for solar panel design, as it establishes that dynamic flutter, rather than static divergence, represents the more restrictive design criterion.

The flutter speed expression reveals several critical design insights:

- *Material dependence:* The $\sqrt{E/\rho}$ term demonstrates that flutter speed scales with the square root of specific stiffness, strongly favouring high-modulus, low-density materials such as carbon fibre composites over traditional aluminium structures.
- *Geometric scaling:* Flutter speed decreases with increasing panel slenderness ratios (η_{p1}, η_{p2}) and mast aspect ratio (γ_m), indicating that structural efficiency gains through material reduction must be carefully balanced against aeroelastic stability requirements.
- *Angular dependence:* The denominator term $\sqrt{\frac{1}{2}\pi \cos(2\alpha) - 0.32\cos(\alpha)}$ shows strong sensitivity to panel inclination, with certain angles being particularly vulnerable to flutter instability.
- *Critical design threshold:* Since flutter occurs before divergence and represents a more realistic failure mode under dynamic loading conditions, it establishes the fundamental wind speed limitation for solar panel operations.

The $\sqrt{E/\rho}$ scaling makes the material selection trade-off immediate. Substituting the canonical values $E = 70$ GPa, $\rho_p = 2700$ kg/m^3 for Aluminium 6061-T4, and $E = 230$ GPa, $\rho_p = 1600$ kg/m^3 for a typical unidirectional CFRP laminate, the corresponding flutter speed ratio is $\sqrt{(230/1600)/(70/2700)} \approx 2.35$. Switching from an aluminium panel to a carbon fibre-reinforced composite panel of the same geometry would therefore raise the predicted flutter wind speed by approximately a factor of 2.3, lifting the predicted flutter onset for a typical configuration from ~35 m/s into the ~80 m/s range and well above the EF-2 tornado wind speeds. This concrete material comparison result, available directly from the closed-form expression, illustrates the value of the analytical framework as a preliminary material selection tool.

Using representative values for aluminium solar panels ($E = 70$ GPa, $\rho_{air} = 1.225$ kg/m^3) and the panel configurations analysed previously, the predicted flutter speeds are: We note that the labels "Type I/II/III" used in the flutter table below denote a local parametric sweep specific to the dynamic flutter analysis, with the η_{p1}, η_{p2} values stated in each row of **Table 2**. As in the divergence analysis (Section 3.2 of Section 3) and the pseudo-static stress analysis (Section 3.1 of Section 3), the same labels are re-used for different parametric ranges and the numerical values associated with each label apply only to the section in which they are introduced.

Table 2. Critical flutter wind speeds for different structural configurations and panel inclination angles, predicted by the closed-form flutter expression in **Equation (75)**. The results indicate that increasing panel inclination or overhang asymmetry leads to an earlier onset of dynamic aeroelastic instability.

Configuration	$\boldsymbol{\theta = 20°}$	$\boldsymbol{\theta = 30°}$	$\boldsymbol{\theta = 45°}$
Type I ($\eta_{p1} = 35, \eta_{p2} = 10$)	42 m/s	36 m/s	28 m/s
Type II ($\eta_{p1} = 45, \eta_{p2} = 15$)	38 m/s	32 m/s	25 m/s
Type III ($\eta_{p1} = 55, \eta_{p2} = 20$)	34 m/s	28 m/s	22 m/s

These flutter speeds are significantly below EF-2 wind speeds (50–60 m/s on the Enhanced Fujita scale of McDonald & Mehta [44]), confirming that dynamic instabilities pose the primary failure mechanism for solar panel systems under extreme wind conditions. The analysis demonstrates that while static divergence provides an upper bound for aeroelastic failure, dynamic flutter represents the more critical and realistic failure mode, occurring at wind speeds that are more likely to be encountered in severe weather events such as the Colorado tornado that destroyed the Pioneer Solar Farm.

Indirect validation of the closed-form predictions is available from four complementary sources, in lieu of a separate experimental campaign for this analytical study. (i) The input pressure coefficients in **Table 1** are consistent with the wind tunnel data of Shademan et al. [37] and the classical flat-plate drag compilation of Hoerner [33], as well as the code-prescribed values in ASCE 7-22 §29.3 [30] and Eurocode EN 1991-1-4 §7.4 [31], and the PV-module qualification testing framework codified in IEC 61215-1:2021 [32]. (ii) The analytical ratio $V_{flutter}/V_{div} = 1/\sqrt{2} \approx 0.707$ coincides with the classical aeroelastic result for single-degree-of-freedom torsional systems [34, 35, 38]. (iii) The predicted flutter wind speeds in **Table 2** (22–42 m/s) are consistent with the wind tunnel tracker-flutter measurements of Taylor et al. [23], Cárdenas-Rondón et al. [21, 22], and Frontini et al. [20] for comparable single-axis tracker geometries. (iv) The predicted dynamic-failure onset range (20–45 m/s) is consistent with the wind speeds reported in the preliminary post-event survey of tornado damage to photovoltaic systems by Okonkwo et al. [1] and with the hurricane-induced damage trends discussed by Patt et al. [2]. The tornado-loading framework of Baker and Sterling [53] and the Enhanced Fujita scale of McDonald and Mehta [44] provide the corresponding mean wind context for events of EF-1/EF-2 intensity, and the FEMA Hazus hurricane technical manual [42] together with the hurricane damage prediction model of Pinelli et al. [43] provide the corresponding hurricane intensity statistics. This flutter analysis provides theoretical insights for configurations operating within the validity range of classical flutter theory, but the fundamental limitations may render it inappropriate for solar panel installations operating at higher inclination angles. Future analytical development should address stall flutter mechanisms relevant to solar panel configurations.

 10.20935/AcadEnergy8386

4. Discussion

The three analytical levels developed in Sections 3.1–3.3 together provide a consistent picture of the failure modes of cantilever-mounted solar panels under wind loading. The pseudo-static analysis identifies the wind speeds at which the mast bending stress and the panel bending stress reach yield (typically $V \sim 50–70$ m/s for the Aluminium 6061-T4/structural steel configurations considered). The static divergence analysis identifies a torsional instability whose critical wind speed is a non-monotonic function of the inclination angle, governed by the moment coefficient derivative $\partial C_M/\partial\alpha$. The dynamic flutter analysis identifies a related but lower critical wind speed, $V_{flutter} = V_{div}/\sqrt{2} \approx 0.707\, V_{div}$, that sets the governing design criterion.

Three points emerge from comparing these three levels. First, the dynamic flutter speed is consistently lower than both the static yield wind speed and the static divergence speed, by a factor of $\sqrt{2}$ relative to divergence and by a larger margin relative to the static yield. The flutter analysis therefore replaces the static yield as the binding design criterion for the configurations of interest. Second, the panel inclination angle plays opposite roles in the static stress and divergence/flutter analyses: steeper angles raise the static stress (because the projected area for the wind pressure increases as $\sin\theta$) but raise the divergence and flutter wind speeds in the attached flow regime ($\alpha \leq 20°$), because $\partial C_M/\partial\alpha$ decreases with α. The two effects must be balanced in design, with the cross-over typically occurring near $\alpha \approx 30°$ for the panel slenderness ratios considered. Third, the material comparison result $V_{flutter} \propto \sqrt{E/\rho}$ identifies the panel-specific stiffness as the most effective design lever: switching from an aluminium panel to a carbon fibre-reinforced composite panel of the same geometry raises the predicted flutter wind speed by approximately a factor of 2.3, lifting a typical ~35 m/s flutter onset to ~80 m/s and above EF-2 wind speeds.

The indirect validation pathways introduced in Section 3.3—consistency of the input pressure coefficients with code-prescribed values (ASCE 7-22 [30], Eurocode EN 1991-1-4 [31], IEC 61215-1:2021 [32]), agreement of the analytical flutter-to-divergence ratio with the classical aeroelastic result, agreement of the predicted flutter wind speeds with the recent tracker-flutter wind tunnel measurements of Taylor et al. [23], Cárdenas-Rondón et al. [21, 22] and Frontini et al. [20], and qualitative agreement with the post-event surveys of tornado and hurricane damage to photovoltaic installations [1, 2, 53]—collectively support the use of the closed-form framework as a preliminary design tool, while the limitations summarised below delineate the regimes in which higher-fidelity numerical or experimental analyses are required.

4.1. Limitations and applicability

The closed-form framework is valid within the assumptions listed at the start of Section 2: cantilever Euler–Bernoulli beam theory for the mast, small-deformation linear elasticity, attached flow flat-plate aerodynamics with $\alpha \lesssim 20°$, uniform mean wind loading, neglect of structural damping (giving a conservative lower bound on the flutter wind speed), and a rigid foundation supporting a single panel. The framework therefore does not directly apply to: (i) multi-column or distributed support PV arrays, where load paths are shared between supports; (ii) large-deformation regimes in which geometric non-linearity becomes important; (iii) installations operating at high inclination angles ($\theta \gtrsim 30°$), where stall-driven flutter mechanisms [48, 54] replace the classical attached flow flutter analysed here; (iv) configurations in which foundation–soil interaction softens the effective torsional stiffness; and (v) turbulent buffeting and fatigue assessment, which require the classical gust-factor or buffeting-analysis frameworks [36, 55]. Within these limits, the closed-form expressions provide a rapid, transparent preliminary design tool that complements (and is expected to be cross-checked against) higher-fidelity CFD, FEM, and wind tunnel analyses. The natural next step for an explicit multi-body/FEM validation of the closed-form k_θ expression, combined with stall flutter aerodynamic models for high-angle installations and the inclusion of turbulent buffeting on the loading side, is suggested by this study.

5. Conclusions

This study has developed an analytical framework for predicting wind-induced failure of solar panel systems by establishing three progressively sophisticated analysis methods: pseudo-static loading, static divergence, and dynamic flutter. The investigation reveals that conventional static design approaches significantly overestimate the wind resistance of solar panels, with dynamic flutter instabilities occurring at wind speeds 30–50% lower than static failure thresholds. Through systematic parametric studies incorporating panel geometry, inclination angles, and material properties, we demonstrate that aeroelastic phenomena, rather than material yielding, govern the survivability of solar installations under extreme wind conditions such as tornadoes and severe storms. The analytical framework provides closed-form analytical expressions for solar panel aeroelastic behaviour within well-defined assumptions, offering a rigorous theoretical foundation for preliminary design assessment and parametric studies.

The research delivers several novel contributions that advance both aeroelastic theory and renewable energy infrastructure design through the development of closed-form expressions:

- The first unified analytical treatment combining mast flexibility with panel aeroelasticity through equivalent torsional stiffness formulations that can reduce dependence on expensive computational fluid dynamics simulations and wind tunnel testing.
- The development of probabilistic fragility curves specifically calibrated for solar panel flutter instabilities, enabling risk-based design methodologies that facilitate real-time assessment of existing installations across diverse wind climatologies.
- The quantification of the critical 0.7 ratio between flutter and divergence speeds for coupled mast–panel systems, providing fundamental scaling relationships previously accessible only through numerical methods.
- The identification of the panel inclination angle as the dominant parameter controlling aeroelastic stability, with closed-form expressions revealing that steeper orientations reduce flutter margins by up to 60%.
- The derivation of explicit analytical dependencies on material properties, geometric parameters, and environmental conditions that provide transparency into failure mechanisms previously obscured within computational black boxes.
- The creation of interpretable mathematical tools that can be directly integrated into design standards, enabling the solar industry to implement science-based wind resistance criteria without specialised expertise or computational resources, ultimately democratising advanced aeroelastic analysis and accelerating the deployment of resilient renewable energy infrastructure worldwide.

These findings establish flutter analysis as an essential design requirement for solar installations, fundamentally shifting design philosophy from strength-based to stability-based criteria.

The practical impact of these results extends to immediate engineering applications in renewable energy infrastructure resilience. Solar farm developers can now implement simple science-based design limits that prevent the kind of catastrophic failures discussed in Section 4, potentially saving millions in equipment losses while maintaining grid reliability during extreme weather. The analytical framework enables rapid assessment of existing installations and optimisation of new designs without expensive wind tunnel testing or computational fluid dynamics at the starting point.

Future research should focus on extending these methods to multi-panel array interactions, developing real-time monitoring systems for flutter onset detection, and investigating active control strategies that could enable safe operation in higher wind speeds, ultimately maximising renewable energy generation while ensuring structural integrity.

Funding

This research was sponsored by the Glasgow University recruitment fund under grant number 30301020/201712-01, and by Renew Risk (London, UK) for S.B.

Author contributions

Conceptualization, S.B.; methodology, S.A.; validation, S.A.; writing—original draft preparation, S.A.; writing—review and editing, S.B.; project administration, S.B.; funding acquisition, S.B. All authors have read and agreed to the published version of the manuscript.

Conflict of interest

Subhamoy Bhattacharya is an employee of Renew Risk (London, UK). The company provided funding for this study, but played no role in the study's conception, design, execution, or interpretation, or with the writing of this manuscript. The authors declare no other financial or personal competing interests.

Data availability statement

All data supporting the findings of this publication are available within this article.

Publisher's note

Copyright

References

1. Okonkwo PC, Nwokolo CS, Udo SO, Obiwulu AU, Onnoghen UN, Alarifi SS, et al. Solar PV systems under weather extremes: Case studies, classification, vulnerability assessment, and adaptation pathways. Energy Rep. 2025; 13: 929–59. doi: 10.1016/j.egyr.2024.12.067

2. Patt A, Pfenninger S, Lilliestam J. Vulnerability of solar energy infrastructure and output to climate change. Clim Chang. 2013; 121 (1): 93–102. doi: 10.1007/s10584-013-0887-0

3. Wu Q, Wang X, He J, Hua X, Chen Z. Study on the flutter characteristics of single-axis solar trackers based on wind tunnel tests of an aeroelastic model. Structures. 2025; 82: 110455. doi: 10.1016/j.istruc.2025.110455

4. Budynas RG, Nisbett JK. Shigley's mechanical engineering design. 8th ed. New York, NY, USA: McGraw-Hill; 2008.

5. Dai SF, Liu HJ, Lam HF, Peng HY. Interference effect of photovoltaic solar arrays on wind load of building roof by large eddy simulations. Eng Struct. 2025; 336: 120453. doi: 10.1016/j.engstruct.2025.120453

6. Wittwer AR, Podestá JM, Castro HG, Mroginski JL, Marighetti JO, De Bortoli ME, et al. Wind loading and its effects on photovoltaic modules: an experimental–computational study to assess the stress on structures. Sol Energy. 2022; 240: 315–28. doi: 10.1016/j.solener.2022.04.061

7. Yemenici O, Aksoy MO. An experimental and numerical study of wind effects on a ground-mounted solar panel at different panel tilt angles and wind directions. J Wind Eng Ind Aerodyn. 2021; 213: 104630. doi: 10.1016/j.jweia.2021.104630

8. Zhang C, Zhao H, Shi G, Wang Q, Wang F, Wang J. Experimental investigation of the flexural performance and photoelectric properties of building integrated photovoltaic (BIPV) laminated glass. Structures. 2025; 81: 110293. doi: 10.1016/j.istruc.2025.110293

9. Ma W, Zhang W, Zhang X, Chen W, Tan Q. Experimental investigations on the wind load interference effects of single-axis solar tracker arrays. Renew Energy. 2023; 202: 566–80. doi: 10.1016/j.renene.2022.11.112

10. Laha SK, Sadhu PK, Dhar RS, Dey R, Bhattacharya S, Ganguly A, et al. Analysis of mechanical stress and structural deformation on a solar photovoltaic panel through various wind loads. Microsyst Technol. 2021; 27 (9): 3465–74. doi: 10.1007/s00542-020-05142-8

11. Aly AM, Clarke J. Wind design of solar panels for resilient and green communities: CFD with machine learning. Sustain Cities Soc. 2023; 94: 104529. doi: 10.1016/j.scs.2023.104529

12. Chen F, Zhu Y, Wang W, Shu Z, Li Y. A review on aerodynamic characteristics and wind-induced response of flexible support photovoltaic system. Atmosphere. 2023; 14 (4): 731. doi: 10.3390/atmos14040731

13. Nan B, Chi Y, Jiang Y, Bai Y. Wind load and wind-induced vibration of photovoltaic supports: a review. Sustainability. 2024; 16 (6): 2551. doi: 10.3390/su16062551

14. Wang J, Van Phuc P, Yang Q, Tamura Y. LES study of wind pressure and flow characteristics of flat-roof-mounted solar arrays. J Wind Eng Ind Aerodyn. 2020; 198: 104096. doi: 10.1016/j.jweia.2020.104096

15. Suárez JL, Cadenas D, Rubio H, Ouro P. Vortex shedding dynamics behind a single solar PV panel over a range of tilt angles in uniform flow. Fluids. 2022; 7 (10): 322. doi: 10.3390/fluids7100322

16. Jubayer CM, Hangan H. Numerical simulation of wind effects on a stand-alone ground mounted photovoltaic (PV) system. J Wind Eng Ind Aerodyn. 2014; 134: 56–64. doi: 10.1016/j.jweia.2014.08.008

17. Jubayer CM, Hangan H. A numerical approach to the investigation of wind loading on an array of ground mounted solar photovoltaic (PV) panels. J Wind Eng Ind Aerodyn. 2016; 153: 60–70. doi: 10.1016/j.jweia.2016.03.009

18. Qin Y, Ke S, Wang B, Ren H, Tian W, Cao J. Research on aeroelastic effect of wind-induced vibration responses of large-span flexible photovoltaic support structure based on wind tunnel experiment comparison of rigid body and aeroelastic model. Sol Energy. 2025; 296: 113605. doi: 10.1016/j.solener.2025.113605

19. Ren H, Liu H, Wang B, Ke S. Spatiotemporal wind pressure field prediction for long-span flexible photovoltaic structures using deep learning and sparse wind tunnel data. Sol Energy. 2025; 286: 113192. doi: 10.1016/j.solener.2024.113192

20. Frontini G, Calamelli F, Muggiasca S, Argentini T. Key parameters influencing wind-induced aeroelastic responses of single-axis solar trackers in photovoltaic plants. Sol Energy. 2025; 287: 113232. doi: 10.1016/j.solener.2024.113232

21. Cardenas-Rondon JA, Ogueta-Gutierrez M, Franchini S, Manzanares-Bercial R. Stability analysis of two-dimensional flat solar trackers using aerodynamic derivatives at different heights above ground. J Wind Eng Ind Aerodyn. 2023; 243: 105606. doi: 10.1016/j.jweia.2023.105606

22. Cardenas-Rondon JA, Gomez-Ortega O, Rodriguez-Casado C, Ogueta-Gutierrez M, Franchini S. Similarity solution for sectional A_2^* aerodynamic derivative for single axis solar trackers at various angles of attack and ground distances. J Wind Eng Ind Aerodyn. 2024; 255: 105932. doi: 10.1016/j.jweia.2024.105932

23. Taylor ZJ, Feero MA, Browne MTL. Aeroelastic instability mechanisms of single-axis solar trackers. J Wind Eng Ind Aerodyn. 2024; 244: 105626. doi: 10.1016/j.jweia.2023.105626

24. Li J, Nie S, Liu M, Yang Q, Hu Q, Guo K, et al. Two parallel cable trusses-supported photovoltaic structure: wind-induced vibration and evaluation of influence factors. Sol Energy. 2025; 299: 113722. doi: 10.1016/j.solener.2025.113722

25. Wu Y, Wu Y, Sun Y, Sun X. Wind-induced vibration response and suppression of the cable-truss flexible support photovoltaic module array. Sol Energy. 2024; 284: 113096. doi: 10.1016/j.solener.2024.113096

26. Bao T, Li Z, Pu O, Chan RWK, Zhao Z, Pan Y, et al. Modal analysis of tracking photovoltaic support system. Sol Energy. 2023; 265: 112088. doi: 10.1016/j.solener.2023.112088

27. Zhu YF, Huang Y, Xu C, Xiao B, Chen CH, Yao Y. Effect of tilt angle on wind-induced vibration in pre-stressed flexible cable-supported photovoltaic systems. Sol Energy. 2024; 277: 112729. doi: 10.1016/j.solener.2024.112729

28. Cai Q, Ke S, Wang L, Ren H, Zhang C, Wu H, et al. Evolution of wind-induced vibration form of large-span flexible PV aeroelastic arrays. Sol Energy. 2024; 277: 112684. doi: 10.1016/j.solener.2024.112684

29. Aly AM. On the evaluation of wind loads on solar panels: the scale issue. Sol Energy. 2016; 135: 423–34. doi: 10.1016/j.solener.2016.06.018

30. American Society of Civil Engineers. Minimum design loads and associated criteria for buildings and other structures. ASCE/SEI 7-22. Reston, VA, USA: American Society of Civil Engineers; 2022.

31. European Committee for Standardization. Eurocode 1: actions on structures—part 1–4: general actions—wind actions (incorporating corrigenda and UK National annex update). BS EN 1991-1-4:2005+A1:2010. Brussels, Belgium/London, UK: CEN/BSI; 2024.

32. International Electrotechnical Commission. Terrestrial photovoltaic (PV) modules—design qualification and type approval—part 1: test requirements. IEC 61215-1:2021. Geneva, Switzerland: IEC; 2021.

33. Hoerner SF. Fluid-dynamic drag: practical information on aerodynamic drag and hydrodynamic resistance. Midland Park, NJ, USA; 1965.

34. Fung YC. An introduction to the theory of aeroelasticity. New York, NY, USA: Dover Publications; 2008.

35. Bisplinghoff RL, Ashley H, Halfman RL. Aeroelasticity. New York, NY, USA: Dover Publications; 1996.

36. Simiu E, Scanlan RH. Wind effects on structures: fundamentals and applications to design. 3rd ed. New York, NY, USA: John Wiley & Sons; 1996.

37. Shademan M, Naghib-Lahouti A. Effects of aspect ratio and inclination angle on aerodynamic loads of a flat plate. Adv Aerodyn. 2020; 2 (1): 38. doi: 10.1186/s42774-020-00038-7

38. Dowell EH. A Modern course in aeroelasticity. 5th ed. Cham, Switzerland: Springer; 2015.

39. Aly AM, Bitsuamlak G. Aerodynamics of ground-mounted solar panels: test model scale effects. J Wind Eng Ind Aerodyn. 2013; 123: 250–60. doi: 10.1016/j.jweia.2013.07.007

40. Hodges DH, Pierce GA. Introduction to structural dynamics and aeroelasticity. 2nd ed. Cambridge, UK: Cambridge University Press; 2011.

41. Ellingwood B, Galambos TV, MacGregor JG, Cornell CA. Probability based load criteria—assessment of current design practice. J Struct Div ASCE. 1982; 108 (5): 959–77. doi: 10.1061/jsdeag.0005958

42. Federal Emergency Management Agency. Hazus hurricane model technical manual. Hazus 5.0. Washington, DC, USA: FEMA Mitigation Division; 2021. Available from: https://www.fema.gov/hazus

43. Pinelli JP, Simiu E, Gurley K, Subramanian C, Zhang L, Cope A, et al. Hurricane damage prediction model for residential structures. J Struct Eng. 2004; 130 (11): 1685–91. doi: 10.1061/(asce)0733-9445(2004)130:11(1685)

44. McDonald JR, Mehta KC. A recommendation for an enhanced Fujita scale (EF-scale). Lubbock, TX, USA: Wind Science and Engineering Center, Texas Tech University; 2006.

45. Meirovitch L. Fundamentals of vibrations. New York, NY, USA: McGraw-Hill; 2001.

46. Ashby MF. Materials and design: the art and science of material selection in product design. 3rd ed. Oxford, UK: Butterworth-Heinemann; 2013.

47. Clough RW, Penzien J. Dynamics of structures. 3rd ed. Berkeley, CA, USA: Computers & Structures Inc.; 2003.

48. Den Hartog JP. Transmission line vibration due to sleet. Trans Am Inst Electr Eng. 1932; 51 (6): 1074–6. doi: 10.1109/ee.1932.6429869

49. Leishman JG. Principles of helicopter aerodynamics. 2nd ed. Cambridge, UK: Cambridge University Press; 2006.

50. Scanlan RH, Tomko JJ. Airfoil and bridge deck flutter derivatives. J Eng Mech Div. 1971; 97 (6): 1717–37. doi: 10.1061/jmcea3.0001526

51. Dixon SL, Hall CA. Fluid mechanics and thermodynamics of turbomachinery. 5th ed. Oxford, UK: Butterworth-Heinemann; 2010.

52. Scanlan RH, Tomko JJ. The action of flexible bridges under wind, I: flutter theory. J Sound Vib. 1978; 60 (2): 187–99. doi: 10.1016/S0022-460X(78)80028-5

53. Baker CJ, Sterling M. Modelling wind fields and debris flight in tornadoes. J Wind Eng Ind Aerodyn. 2017; 168: 312–21. doi: 10.1016/j.jweia.2017.06.017

54. Parkinson GV, Smith JD. The square prism as an aeroelastic non-linear oscillator. Q J Mech Appl Math. 1964; 17 (2): 225–39. doi: 10.1093/qjmam/17.2.225

55. Baker CJ. The simulation of unsteady aerodynamic cross wind forces on trains. J Wind Eng Ind Aerodyn. 2010; 98 (2): 88–99. doi: 10.1016/j.jweia.2009.09.006